



Available online at [www.sciencedirect.com](http://www.sciencedirect.com)

**ScienceDirect**

Comput. Methods Appl. Mech. Engrg. 387 (2021) 114169

**Computer methods  
in applied  
mechanics and  
engineering**

[www.elsevier.com/locate/cma](http://www.elsevier.com/locate/cma)

# A general SPH framework for transient seepage flows through unsaturated porous media considering anisotropic diffusion

Yanjian Lian<sup>a</sup>, Ha H. Bui<sup>a,\*</sup>, Giang D. Nguyen<sup>b</sup>, Hieu T. Tran<sup>a</sup>, Asadul Haque<sup>a</sup>

<sup>a</sup> Department of Civil Engineering, Monash University, Melbourne, Australia

<sup>b</sup> School of Civil, Environmental & Mining Engineering, University of Adelaide, Adelaide, Australia

Received 3 June 2021; received in revised form 23 August 2021; accepted 31 August 2021

Available online 2 October 2021

## Abstract

The Smoothed Particle Hydrodynamics (SPH) method has become a popular numerical tool to solve many challenging engineering applications. However, its application to solving anisotropic transient unsaturated–saturated seepage flow problems is still absent in the literature. Among several challenges involved in solving this important problem, the lack of a robust and general SPH formulation to obtain accurate approximations of second derivatives on disordered particle system is the key obstacle preventing this to happen. In this paper, we first propose a general SPH formulation for the second derivatives, capable of considering anisotropic diffusions, and demonstrate that the new formulation outperforms existing SPH formulations for the second derivatives and achieves high accuracy on the highly disordered particle systems. Subsequently, we utilise this newly developed SPH formulation to tackle the transient seepage flows through porous media for the first time, considering anisotropic flows and complete time-dependent transition from unsaturated to saturated states and vice-versa. This naturally leads to a general SPH framework for solving transient seepage problems in unsaturated/saturated porous media using one set of Lagrangian particles (or Lagrangian discretisation). Robust boundary conditions and their implementations for solving general seepage problems in SPH are also proposed, enabling the proposed SPH model to automatically capture seepage surface (including the free surface of unconfined seepage) without any difficulty or ad hoc treatment. Moreover, a simple method to generate a random particle system suitable for SPH simulations on large scale problems using the Voronoi tessellation technique is proposed to study transient seepage problems for the first time. Several verification examples are presented to demonstrate the capabilities of the proposed SPH framework in solving the complex seepage flow problems, including those on multi-resolution particle configurations. Excellent agreements with a wide range of numerical and theoretical solutions are achieved, suggesting that the newly proposed SPH model can be applied to solve complex transient seepage flow problems. This marks an important milestone for the future development of SPH to solve fully coupled flow deformation problems involved large deformation and failure of porous media, which are challenging for the most state-of-the-art mesh-based numerical methods.

© 2021 Elsevier B.V. All rights reserved.

**Keywords:** SPH; Transient seepage; Anisotropic diffusion; Unsaturated media; Voronoi tessellation

\* Corresponding author.

E-mail address: [ha.bui@monash.edu](mailto:ha.bui@monash.edu) (H.H. Bui).

## 1. Introduction

Seepage flow through unsaturated porous media is a particularly important topic in engineering, including geotechnical engineering, environmental engineering and agricultural engineering. Unsaturated seepage flow occurring in the soil media may significantly change soil properties (e.g., suction, water content and shear strength), which would subsequently influence the performance and safety of geo-infrastructures or even lead to severe damages and catastrophic disasters. A better understanding and prediction of seepage behaviour is significantly essential to prevent these failures occur. Thus, the topic of numerical studies on the seepage flow through unsaturated media is still very active in recent years.

Among many existing numerical tools, the Finite Element Method (FEM) is perhaps one of the most popular methods, which has been successfully used to solve seepage problems [1]. One of the main challenges for FEM is to locate the position of the phreatic line [1–3], which also often refers to as the seepage surface. The position of seepage surface in FEM is unknown in advance, and thus numerical iterations or extra treatments are required to properly locate the free surface. Two popular methods, namely mesh adaption technique [4,5] and fixed-mesh method associated with extra variational inequalities equations [6–9], have been adopted in FEM to locate seepage surface boundary. In the former approach, the problem domain needs to be re-meshed at each step of the iteration. As this iterative process requires extra computation costs and may even lead to numerical convergence problems, the latter approach is often adopted. However, the accuracy of both approaches is still highly dependent on the mesh construction and often lead to divergent problems when strong inhomogeneity and complex geometry involved [2,3]. Recently, new proposals of the variational inequality formulations or unilateral constraint conditions within the fixed-mesh method for the free-seepage surface boundary have been reported in the literature [1–3,10]. However, these new treatments still require high computation costs, and thus there is still a need to develop new and robust techniques for FEM to locate the seepage surface more effectively. On the other hand, for more complex seepage problems involved in large deformation of the porous media, this mesh-based FE method may encounter another difficulty associated with severe mesh distortion issues [11]. From this point of view, mesh-free methods might be another better choice if they could handle well the seepage problems.

Smoothed Particle Hydrodynamics (SPH) is the eldest and truly mesh-free method, which is originally developed for astrophysical applications [12,13]. Since its invention, SPH has gained significant popularity in a wide range of engineering applications, such as fluid dynamics problems [14–21], fluid–structure interactions [16,22–30] and solid mechanics [31]. The first SPH framework for modelling the elastoplastic behaviour of geomaterials was presented in [32]. Subsequently, this framework was widely used to solve a range of challenging geotechnical problems, for example, granular flows [33–38], slope failures [39–45], soil–structure interactions [46–49], desiccation cracking in soils [50,51] and rock fractures [52–54]. The application of SPH to solve soil–water interaction problems in fully saturated soils have also been proposed [11,41,55,56], and most of which are based on the original two-phase SPH model [57] in which solid and fluid phases are solved simultaneously using two different sets of Lagrangian particles. Despite such increasing popularity of SPH, its application to solving anisotropic unsaturated–saturated seepage flow problems is still absent in the literature. Among several existing challenges involved in solving this complex seepage problem, the lack of a robust and general SPH formulation to obtain accurate approximations for the second derivatives on a random particle system is the key obstacle, particularly for problems involving anisotropic diffusions. For example, there exist robust SPH formulations for the approximation of second derivatives [58–64], which yield reasonable accuracy on regular particle systems. However, the accuracy of these formulations is considerably degraded on the random or disordered particle system, which prevents them from obtaining general solutions for diffusion problems or for large scale applications where variable discretisations of problem domain are required. Recently, an attempt has been made to produce a highly accurate SPH formulation for the approximation of the Laplacian operator on both regular and highly random particle systems [65,66]. However, this latest SPH formulation was only proposed for the Laplacian operator, and thus could not be used to solve anisotropic seepage problems that involve individual second-order derivatives terms. As a result, there still a need to develop a robust and general SPH scheme for the approximation of second-order derivatives, which can be used to solve anisotropic diffusion problems.

Besides the need to address issues related to the accuracy of SPH approximation for anisotropic seepage flows through porous media, another problem one might concern about is the computational cost, which leads to another topic of interest in this paper, that is, how to solve large-scale seepage problems with cheaper computational costs

using SPH. In the conventional SPH method, particles are popularly arranged in a cubic lattice due to their well-known interpolation accuracies and ease of setup [67]. However, this uniform particle configuration may perform less efficiently and requires higher computational costs for large-scale applications. From this point of view, a spatially multi-resolution discretisation might be more suitable for large scale seepage problems, though this again requires robust and accurate SPH approximations suitable for variable resolutions or random particles in general. Therefore, a robust and simple method to generate a multi-resolution particle system suitable for SPH simulations is also required. It is worth noting that multi-resolution particle systems have been popularly adopted in SPH applications for astrophysics [16,68–71] and fluid dynamics [20,30], but none of them is available for large scale geomechanics applications.

This paper aims to address all the above technical challenges associated with SPH to develop a general SPH framework for anisotropic transient seepage flow through unsaturated porous media. First, a general SPH formula for the approximation of second-order derivatives considering anisotropic diffusions is developed. Subsequently, this new SPH formulation is utilised to solve anisotropic transient seepage flows through porous media for the first time, considering the complete time-dependent transition from unsaturated to saturated states and vice-versa. Robust treatments of boundary conditions and their implementations for solving general seepage problems are also proposed to demonstrate that, unlike FEM, SPH does not require complex treatments for seepage surface boundary conditions. Even with simple treatment, the proposed SPH model could automatically capture the seepage surface, including the free surface of the unconfined seepage, without any difficulty or ad hoc treatment regardless of the complexity of the problem geometry. Meanwhile, a simple method to generate a random particle system with spatially multi-resolution suitable for SPH simulations of large-scale problems using the Voronoi tessellation technique is proposed to study transient seepage problems for the first time. Finally, several verification examples are presented to demonstrate the capabilities of the proposed SPH framework in solving the complex seepage flow problems, including those on multi-resolution particle configurations.

## 2. Multi-phase flow framework

Due to the complex nature of unsaturated soils, it is necessary to impose certain simplifications and assumptions before a numerical analysis can be performed. In the current multi-phase flow framework, the following assumptions are used:

1. *No mass exchange among phase components;*
2. *The process is isothermal.*
3. *Diffusive terms in liquid and air are neglected.*
4. *Terzaghi's effective stress concept is accepted.*

With the above assumptions, the general mass and momentum balances for a three-phase system can be derived and will be revisited in detail in the following sections to facilitate the development of appropriate SPH formulations and boundary conditions.

### 2.1. Definitions of partial density and partial stress in the unsaturated porous medium

The unsaturated porous media considered herein is a three-phase mixture consisting of a soil skeleton, a water phase, and an air phase. The pore-space inside the soil skeleton is assumed to be fully occupied by water and air. In the current approach, the porous media is represented using a single set of Lagrangian SPH particles, over which the information on each phase is described. A representative volume of such an unsaturated porous medium can be illustrated in Fig. 1. This representative volume ( $\Omega$ ) can be further subdivided into three intrinsic phases, including a solid volume ( $\Omega_s$ ), a liquid volume ( $\Omega_l$ ), and an air volume ( $\Omega_a$ ), such that  $\Omega = \Omega_s + \Omega_l + \Omega_a$ . Next, a homogenisation process is applied by assuming that each phase component will occupy the entire volume  $\Omega$ . The governing equations of each phase are subsequently written for its homogenised volume. Finally, the complete governing equations for a three-phase system can be established by combining the governing equations of each homogenised phase. Accordingly, the partial densities of each phase in the porous media are respectively defined as:

$$\bar{\rho}_\alpha = n_\alpha \rho_\alpha \quad n_s + n_l + n_a = 1 \quad (1)$$

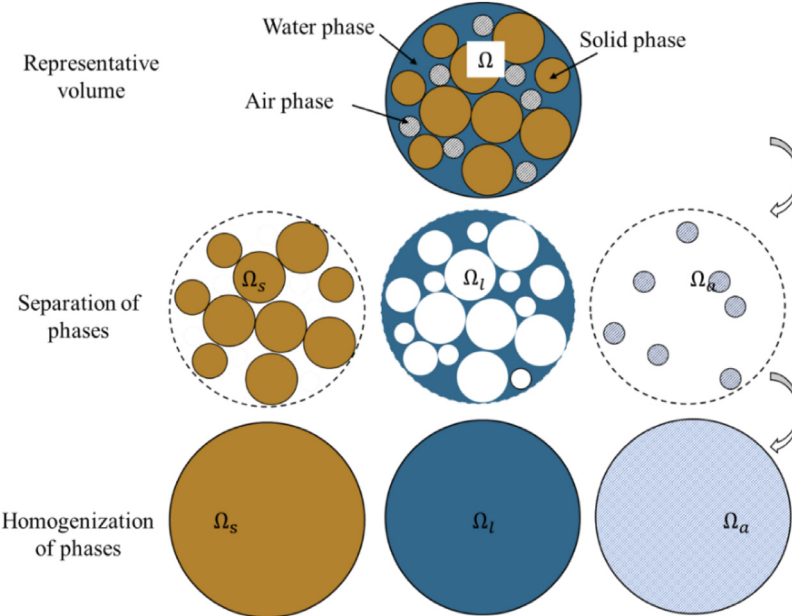


**Fig. 1.** Schematic diagram of a representative volume  $\Omega$  of an unsaturated porous medium and its decomposition into three intrinsic phases (i.e. soil, water and air) and their homogenisations.

where letter  $\alpha$  denotes phase component, with  $s$ ,  $l$  and  $a$  being soil, liquid and air phases, respectively;  $\rho_\alpha$  is the intrinsic mass density of each constituent, and  $n_\alpha$  is the void fraction (or volume fraction) of each phase, which can be explicitly written as:

$$n_s = 1 - n \quad n_l = n S_r \quad n_a = n (1 - S_r) \quad (2)$$

with  $n$  and  $S_r$  being the porosity and the degree of saturation, respectively.

Using the above definitions of partial density, the total density of the three-phase mixture ( $\rho_t$ ) can be expressed as:

$$\rho_t = \bar{\rho}_s + \bar{\rho}_l + \bar{\rho}_a \quad \bar{\rho}_s = n_s \rho_s \quad \bar{\rho}_l = n_l \rho_l \quad \bar{\rho}_a = n_a \rho_a \quad (3)$$

Similar to the density, the partial stresses of each phase in a three-phase system can be defined as:

$$\boldsymbol{\sigma} = \bar{\boldsymbol{\sigma}}_s + \bar{\boldsymbol{\sigma}}_l + \bar{\boldsymbol{\sigma}}_a \quad \bar{\boldsymbol{\sigma}}_s = n_s \boldsymbol{\sigma}_s \quad \bar{\boldsymbol{\sigma}}_l = -n_l p_l \mathbf{I} \quad \bar{\boldsymbol{\sigma}}_a = -n_a p_a \mathbf{I} \quad (4)$$

where  $\boldsymbol{\sigma}_\alpha$  is the intrinsic stress tensor of component  $\alpha$ ;  $\mathbf{I}$  is the unit tensor;  $\boldsymbol{\sigma}$  is the total stress tensor of the three-phase mixture, which is the sum of the partial stress of each phase  $\bar{\boldsymbol{\sigma}}_\alpha$ ;  $p_l$  and  $p_a$  are the pore-water and pore-air pressures, respectively. In this paper, the negative sign of pressures or stresses indicates compression. Using Eqs. (2) and (4), the partial stress tensor of soil in terms of skeleton stress also can be defined as follows:

$$\bar{\boldsymbol{\sigma}}_s = \boldsymbol{\sigma}' - (1 - n) p^F \mathbf{I} \quad p^F = S_r p_l + (1 - S_r) p_a \quad (5)$$

where  $\boldsymbol{\sigma}'$  is the skeleton stress tensor (or effective stress tensor), whose negative sign indicates compression, and  $p^F$  is the average pore pressure. From Eqs. (4)–(5), the following definition of effective stress tensor can be obtained:

$$\boldsymbol{\sigma}' = \boldsymbol{\sigma} + p^F \mathbf{I} \quad (6)$$

## 2.2. Mass balance of the unsaturated mixture

The mass balance equation for each phase in a unit volume consisting of solid, fluid and air phases can be obtained by enforcing the material derivative of each corresponding phase mass in the unit volume to zero, as

shown in Bui & Nguyen [11], this leads to the following equations:

$$\frac{d^\alpha \bar{\rho}_\alpha}{dt} + \bar{\rho}_\alpha \nabla \cdot \mathbf{v}_\alpha = 0 \quad \text{and} \quad \frac{d^\alpha \pi}{dt} = \frac{\partial \pi}{\partial t} + \mathbf{v}_\alpha \cdot \nabla \pi \quad (7)$$

where  $\mathbf{v}_\alpha$  is the velocity vector of phase  $\alpha$  in the mixture; and  $(d^\alpha/dt)$  denotes the material derivative of a field quantity ( $\pi$ ) on phase  $\alpha$ .

Let us first consider the mass balance of the soil phase. The rate of change of local porosity can be obtained by substituting Eq. (1) into Eq. (7):

$$\frac{d^s n}{dt} = (1 - n) \nabla \cdot \mathbf{v}_s + \hat{\alpha} \frac{d^s p_l}{dt} \quad (8)$$

where  $\hat{\alpha} = (1 - n)/K_s$  is the compressibility of the soil skeleton, with  $K_s$  being the bulk modulus of the soil skeleton, and the last term in Eq. (8) was obtained by enforcing the following condition,  $\frac{1}{\rho_s} \frac{d^s \rho_s}{dt} = \frac{1}{K_s} \frac{d^s p_l}{dt}$ .

Similarly, the following mass balance equations for water and air phases can be obtained by making uses of Eq. (3):

$$n_l \frac{d^l \rho_l}{dt} + n \rho_l \frac{d^l S_r}{dt} + \rho_l S_r \frac{d^l n}{dt} = -n_l \rho_l \nabla \cdot \mathbf{v}_l \quad (9)$$

$$n_a \frac{d^a \rho_a}{dt} - n \rho_a \frac{d^a S_r}{dt} + \rho_a (1 - S_r) \frac{d^a n}{dt} = -n_a \rho_a \nabla \cdot \mathbf{v}_a \quad (10)$$

It is noted that Eqs. (9) and (10) are written on the material reference frame of water and air phases, respectively. In this work, since all information of water and air phases are carried on the solid phase, it is important to rewrite the above equations on the soil reference frame. This can be achieved by making use of Eq. (7) to convert the material derivatives of a field quantity on the water and air phases to those on the solid phase, leading to the following equations:

$$n_l \left( \frac{d^s \rho_l}{dt} + \bar{\mathbf{w}}_{ls} \cdot \nabla \rho_l \right) + n \rho_l \left( \frac{d^s S_r}{dt} + \bar{\mathbf{w}}_{ls} \cdot \nabla S_r \right) + \rho_l S_r \left( \frac{d^s n}{dt} + \bar{\mathbf{w}}_{ls} \cdot \nabla n \right) = -n_l \rho_l \nabla \cdot \mathbf{v}_l \quad (11)$$

$$\begin{aligned} n_a \left( \frac{d^s \rho_a}{dt} + \bar{\mathbf{w}}_{as} \cdot \nabla \rho_a \right) - n \rho_a \left( \frac{d^s S_r}{dt} + \bar{\mathbf{w}}_{as} \cdot \nabla S_r \right) + \rho_a (1 - S_r) \left( \frac{d^s n}{dt} + \bar{\mathbf{w}}_{as} \cdot \nabla n \right) \\ = -n_a \rho_a \nabla \cdot \mathbf{v}_a \end{aligned} \quad (12)$$

where the relative velocity between two phases is defined as  $\bar{\mathbf{w}}_{\alpha\beta} = \mathbf{v}_\alpha - \mathbf{v}_\beta$ . Under the same reference frame, substituting Eq. (8) into Eqs. (11) and (12) yields:

$$\frac{n_l}{\rho_l} \left( \frac{d^s \rho_l}{dt} + \bar{\mathbf{w}}_{ls} \cdot \nabla \rho_l \right) + n \left( \frac{d^s S_r}{dt} + \bar{\mathbf{w}}_{ls} \cdot \nabla S_r \right) + S_r \hat{\alpha} \frac{d^s p_l}{dt} + S_r \nabla \cdot \mathbf{v}_s + \nabla \cdot (n S_r \bar{\mathbf{w}}_{ls}) = 0 \quad (13)$$

$$\frac{n_a}{\rho_a} \left( \frac{d^s \rho_a}{dt} + \bar{\mathbf{w}}_{as} \cdot \nabla \rho_a \right) - n \frac{d^s S_r}{dt} + (1 - S_r) \hat{\alpha} \frac{d^s p_l}{dt} + (1 - S_r) \nabla \cdot \mathbf{v}_s + \nabla \cdot (n_a \bar{\mathbf{w}}_{as}) = 0 \quad (14)$$

The rate of change of water density per unit volume in Eq. (13) can be related to the pore-water pressure ( $p_l$ ) by enforcing the following linear relationship between ( $p_l$ ) and volumetric strain of water ( $\varepsilon_l^v$ ):

$$\frac{1}{\rho_l} \frac{d^s \rho_l}{dt} = -\frac{1}{V_l} \frac{d^s V_l}{dt} = -\left( \frac{d^s \varepsilon_l^v}{dt} \right) = \underbrace{\left( K_l^{sat} \right)^{-1}}_{\hat{\beta}} \frac{d^s p_l}{dt} \quad (15)$$

where  $K_l^{sat}$  is the volumetric elastic coefficient of pore fluid, and  $\hat{\beta}$  is the compressibility of pore fluid. Substituting Eq. (15) into Eq. (13), the mass balance equation for the liquid phase component in the three-phase mixture can be finally expressed as:

$$\underbrace{\left( n_l \hat{\beta} + \hat{\alpha} \right)}_{m_v} \frac{d^s p_l}{dt} + n_l \bar{\mathbf{w}}_{ls} \cdot \nabla \rho_l + n \frac{d^s S_r}{dt} + S_r \nabla \cdot \mathbf{v}_s + \nabla \cdot (n_l \bar{\mathbf{w}}_{ls}) = 0 \quad (16)$$

where  $m_v$  is the coefficient of volume change. Similarly, the rate change of air density per unit volume in Eq. (14) can be expanded using the chain rule and ideal gas law as follows:

$$\frac{d^s \rho_a}{dt} = \frac{1}{RT} \frac{d^s p_a}{dt} + \frac{1}{RT} \frac{d^s (T^{-1})}{dt} \quad (17)$$

where  $R$  is the specific gas constant for dry air and  $T$  is the temperature. By enforcing the isothermal assumption, the second term on the right-hand side of Eq. (17) can be neglected, and thus the mass balance equation for the air phase becomes:

$$\frac{n_a}{\rho_a} \left( \frac{1}{RT} \frac{d^s p_a}{dt} + \bar{\mathbf{w}}_{as} \cdot \nabla \rho_a \right) - n \frac{d^s S_r}{dt} + \rho_a (1 - S_r) \hat{\alpha} \frac{d^s p_l}{dt} + \frac{n_a}{n} \nabla \cdot \mathbf{v}_s + \nabla \cdot (n_a \bar{\mathbf{w}}_{as}) = 0 \quad (18)$$

Finally, to finalise Eqs. (16) and (18), one needs the relative velocities between water–soil phases  $\bar{\mathbf{w}}_{ls}$  and between air–soil phases  $\bar{\mathbf{w}}_{as}$ , respectively. These relative velocities can be obtained by considering the momentum balances of the mixture, which will be derived in the next section.

### 2.3. Momentum balance of the unsaturated mixture

The behaviour of unsaturated porous media is governed by the interaction between solid skeleton and pore-fluids, each of which is considered as a homogenised continuum that follows its governing equations. Thus, the general form of the linear momentum for each phase component in the three-phase mixture can be written as follows:

$$\bar{\rho}_\alpha \frac{d^\alpha \mathbf{v}_\alpha}{dt} = \nabla \cdot \bar{\boldsymbol{\sigma}}_\alpha + \bar{\rho}_\alpha \mathbf{b} - \sum \mathbf{R}^{\alpha\beta} \quad (19)$$

where  $\mathbf{b} = [0 \quad -g]$  is the gravitational force vector; and  $\mathbf{R}^{\alpha\beta}$  is the interaction drag force vector between phase  $\alpha$  and  $\beta$ , which can take the following form based on the linear Darcy's law [11]:

$$\mathbf{R}^{\alpha\beta} = \frac{\bar{\rho}_\alpha g}{\mathbf{k}_\alpha} n_\alpha \bar{\mathbf{w}}_{\alpha\beta} + p_\alpha \nabla n_\alpha \quad (20)$$

where  $\mathbf{k}_\alpha \equiv k^{mn} \delta^{mn}$  is the permeability coefficient tensor of phase  $\alpha$ , with  $m$  and  $n$  indicating the coordinate. It is noted here that the spatial derivatives of porosity and the degree of saturation are considered sufficiently small, thus can be neglected [72,73].

To define the relative velocities between the water/air phases to that of the solid phase, Eq. (19) can be written for the liquid and air phases as follows:

$$\bar{\rho}_l \frac{d^s \mathbf{v}_s}{dt} = \nabla \cdot \bar{\boldsymbol{\sigma}}_l + \bar{\rho}_l \mathbf{b} - \mathbf{R}^{ls} - \mathbf{R}^{la} \quad (21)$$

$$\bar{\rho}_a \frac{d^s \mathbf{v}_s}{dt} = \nabla \cdot \bar{\boldsymbol{\sigma}}_a + \bar{\rho}_a \mathbf{b} - \mathbf{R}^{as} - \mathbf{R}^{al} \quad (22)$$

By substituting the definitions of partial stress tensors for the water and air phases and the interaction drag force into Eqs. (21) and (22), and neglecting the interaction forces between water and air phases (i.e., Assumption 3), the relative velocities between liquid and air phases to the soil skeleton can be written as follows, respectively:

$$\bar{\mathbf{w}}_{ls} = \frac{\mathbf{k}_l}{n_l \gamma_l} \left( -\nabla p_l + \rho_l \mathbf{b} - \rho_l \frac{d^s \mathbf{v}_s}{dt} \right) \quad (23)$$

$$\bar{\mathbf{w}}_{as} = \frac{\mathbf{k}_a}{n_a \gamma_a} \left( -\nabla p_a + \rho_a \mathbf{b} - \rho_a \frac{d^s \mathbf{v}_s}{dt} \right) \quad (24)$$

### 2.4. Flow equations for the unsaturated seepage flow through rigid porous media

The general equations governing the unsaturated seepage flow through porous media can be now obtained by combining the mass and momentum conservation equations described in the earlier sections. This can be achieved by substituting Eqs. (23) and (24) into Eqs. (16) and (18), respectively, which yields:

$$m_v \frac{d^s p_l}{dt} + n_l \bar{\mathbf{w}}_{ls} \cdot \nabla \rho_l + n \frac{d^s S_r}{dt} + S_r \nabla \cdot \mathbf{v}_s + \frac{1}{\gamma_l} \nabla \cdot \left[ \mathbf{k}_l \left( -\nabla p_l + \rho_l \mathbf{b} - \rho_l \frac{d^s \mathbf{v}_s}{dt} \right) \right] + \bar{\mathbf{w}}_{ls} \cdot \nabla n = 0 \quad (25)$$

$$\begin{aligned} \frac{n_a}{\rho_a} \left( \frac{1}{RT} \frac{d^s p_a}{dt} + \bar{\mathbf{w}}_{as} \cdot \nabla \rho_a \right) - n \frac{d^s S_r}{dt} + \rho_a (1 - S_r) \hat{\alpha} \frac{d^s p_l}{dt} + \frac{n_a}{n} \nabla \cdot \mathbf{v}_s \\ + \frac{1}{\gamma_a} \nabla \cdot \left[ \mathbf{k}_a \left( -\nabla p_a + \rho_a \mathbf{b} - \rho_a \frac{d^s \mathbf{v}_s}{dt} \right) \right] = 0 \end{aligned} \quad (26)$$

Eqs. (25) and (26) describe the rate of change of pore-water and pore-air pressures in the unsaturated porous media, respectively. They are, in principle, can be solved using any appropriate numerical method if a hydraulic constitutive model, which links the degree of saturation to the pore-water and pore-air pressures, is provided. In this paper, in an attempt to establish the first SPH framework to describe the transient behaviour of unsaturated seepage flows through porous media under complex boundary conditions, a simplified version of the above flow equations is considered. In particular, in the remainder of this paper, we will assume the soil phase is not deformable ( $\mathbf{v}_s = 0$ ) and disregard the gas phase (i.e.,  $p_a = 0$ ). We also assume that the spatial gradient of water density is negligible [72,73]. Furthermore, all the material derivatives in the remainder of this paper will be taken with respect to the soil reference frame, and thus the subscript “*s*” will be dropped to simplify our mathematical expressions. At the same time, the subscript “*l*” for the variables of the liquid phase (i.e.,  $\mathbf{k}_l$ ,  $h_l$  and  $H_l$ ) will be dropped. Accordingly, the above general equations for the transient unsaturated seepage flow through a porous medium reduce to the following equation:

$$m_v \frac{dp_l}{dt} + n \frac{dS_r}{dt} + \frac{1}{\gamma_l} \nabla \cdot [\mathbf{k}(-\nabla p_l + \rho_l \mathbf{b} \nabla z)] = 0 \quad (27)$$

Eq. (27) can be recast in terms of water-pressure head ( $h = \frac{p_l}{\gamma_l}$ ) or hydraulic-head ( $H = \frac{p_l}{\gamma_l} + z$ ), with  $z$  being the elevation, by adopting the incompressibility condition of the intrinsic water phase. This leads to the following general water-pressure head equation to describe the transient unsaturated seepage flow:

$$C_l \frac{dh_l}{dt} + n \frac{dS_r}{dt} = \nabla \cdot [\mathbf{k} \nabla (h + z)] \quad (28)$$

where  $C_l (K_s, K_l^{sat}) = \gamma_l m_v$  is the specific storage term and  $\mathbf{q} = \mathbf{k} \nabla (h + z)$  is known as the specific discharge tensor obeying Darcy's law. The second term on the left-hand side of Eq. (28) can be related to the time rate of the water-pressure head by applying the chain rule, which leads to the following equation for the increment of water-pressure head:

$$\frac{dh_l}{dt} = \frac{1}{\tilde{C}_{Sr}} \nabla \cdot [\mathbf{k} \nabla (h + z)] \quad (29)$$

where

$$\tilde{C}_{Sr} = (C_l + C_s) \quad \text{with} \quad C_s = n \frac{dS_r}{dh} \quad (30)$$

To complete the above equation, a hydraulic constitute model is required to calculate the specific moisture term  $C_s(h, S_r)$ . This can be achieved using the hydraulic constitutive model described in the next Section 2.5, and incorporating it into the above governing equation.

## 2.5. Hydraulic constitutive model

There exist many hydraulic models that can be used to describe the hydraulic behaviour of unsaturated soils [74]. Among these models, the van-Genuchten model [75] is the most widely used water retention (SWRC) model and thus is adopted in this paper in an attempt to establish the first SPH framework to describe the transient unsaturated seepage flow through a porous medium. The van-Genuchten SWRC model is a three-parameter equation and relates the degree of saturation ( $S_r$ ) to the suction head ( $-h$ ) as follows [75]:

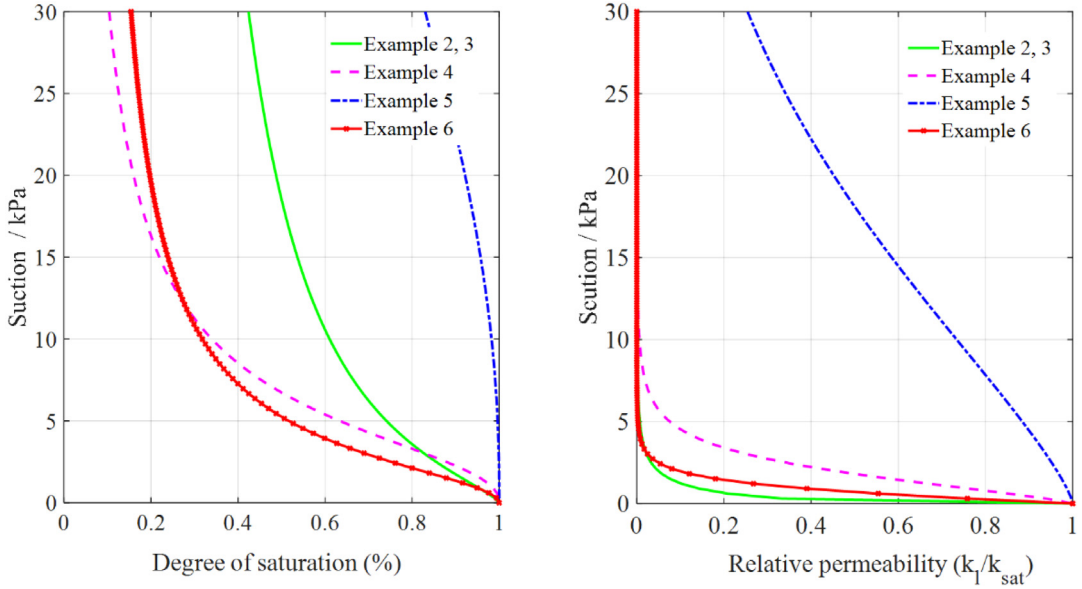
$$S_r = S_{res} + (S_{sat} - S_{res}) [1 + (g_a | -h |)^{g_n}]^{g_c} \quad (31)$$

where  $S_{res}$  is the residual degree of saturation and is used to describe the amount of water that remains in the soil at a high suction head;  $S_{sat}$  is the degree of saturation when the pores are fully filled with water;  $g_a$ ,  $g_n$  and  $g_c = \frac{1-g_n}{g_n}$  are empirical parameters used to fit the van-Genuchten model to different types of soil with different hydraulic properties.

**Table 1**

Parameters for SWRC and water conductivity model.

Example	2, 3	4	5	6
Saturated permeability, $k_{sat}$	1.00 m/day	1.00 m/day	$10^{-9}, 0.1, 1$ m/s	0.047 m/min
Peak saturation, $S_{sat}$	1.00	1.00	1.00	1.00
Residual saturation, $S_{res}$	0.0625	0.02	0.02	0.0623
The SWCC parameter, $g_a$	$3.383 \text{ m}^{-1}$	$2.24 \text{ m}^{-1}$	$0.224 \text{ m}^{-1}$	$3.73 \text{ m}^{-1}$
The SWCC parameter, $g_n$	1.3774	2.286	2.286	1.96
The SWCC parameter, $g_l$	1.2500	0.0	0.0	2.25
Porosity of soil, $n$	0.36	0.36	0.36	0.6
Young's modulus, $E$	300 kPa	300 kPa	300 kPa	1000 kPa
Elastic coefficient of pore fluid	$2.0 \times 10^6$ kPa	$2.0 \times 10^6$ kPa	$2.0 \times 10^6$ kPa	$2.0 \times 10^6$ kPa

**Fig. 2.** Soil water characteristic curve and water conductivity model used in Examples 2 to 5.

In addition to the SWRC model, a water conductivity model that links the hydraulic conductivity of unsaturated soil to its degree of saturation is also required. Here, we adopt the Mualem–van Genuchten’s water conductivity model [75], which links the water conductivity to the effective degree of saturation ( $S_e$ ) and is written as follows:

$$\mathbf{k} = \mathbf{k}^{sat} S_e^{g_l} \left[ 1 - \left( 1 - S_e^{-\frac{1}{g_c}} \right)^{-g_c} \right]^2 \quad (32)$$

where  $\mathbf{k}^{sat} \equiv k^{sat} \delta^{mn}$  is the water conductivity under the fully saturated condition, and the effective degree of saturation can be defined as  $S_e = (S_r - S_{res}) / (S_{sat} - S_{res})$ .

**Fig. 2** shows the Van-Genuchten SWRC model and the Mualem–van Genuchten’s water conductivity model following Eqs. (31) and (32) for four different types of soil. These hydraulic models will be subsequently used in Section 5 to verify the performance of our newly developed SPH framework (i.e. Examples 2 to 6). Parameters required for these hydraulic models are listed in **Table 1**, while other parameters required for special cases solved in Examples 1 will be given in the corresponding sections. For all example considered in this paper, the following material properties are adopted: water density of  $1000 \text{ kg/m}^3$ ; soil density of  $2000 \text{ kg/m}^3$ .

### 3. SPH approximations of the seepage flow equations

#### 3.1. Fundamental SPH formulations

SPH is a continuum Lagrangian numerical method in which the computation domain is discretised into a finite number of particles, with each particle carrying field variables such as mass, density, velocity and pressure [32]. These variables and their gradients at a given particle are then calculated through an integral process that makes use of information from its surrounding particles weighted by a kernel function. Consider an arbitrary field function  $f(\mathbf{x})$  at any point  $\mathbf{x}_i$  in the computational domain, the SPH approximation of this function at  $\mathbf{x}_i$  can be written as follows:

$$\langle f(\mathbf{x}_i) \rangle = \sum_{j=1}^N V_j f(\mathbf{x}_j) W(\mathbf{x}_i - \mathbf{x}_j, \hbar_{sml}) \quad (33)$$

The angle bracket  $\langle \rangle$  indicates the kernel approximation operator;  $V_j$  is the volume occupied by particle  $j$ ;  $W(\mathbf{x}_i - \mathbf{x}_j, \hbar_{sml})$  is the weighted (or kernel) function, with a characteristic length  $\hbar_{sml}$  (also known as the smoothing length) defining an effective domain  $\Omega$  of the kernel function. Among several popular kernel functions in the literature, the cubic-spline kernel function is adopted in this paper and taken the following form [76]:

$$W(q) = \alpha_d \begin{cases} \frac{2}{3} - q^2 + \frac{1}{2}q^3, & 0 \leq q < 1 \\ \frac{1}{6}(2-q)^3, & 1 \leq q < 2 \\ 0, & q \geq 2 \end{cases} \quad (34)$$

where  $\alpha_d$  is a dimensional normalising factor, which is equal to  $1/\hbar_{sml}$  for 1D problems and  $15/7\pi\hbar_{sml}^2$  for 2D problems; and  $q$  is the normalised distance defined as  $q = |\mathbf{x}_i - \mathbf{x}_j| / \hbar_{sml}$ .

Eq. (33) is the fundamental SPH approximation formulation and could be used to derive any existing SPH formulation available in the literature. For example, the SPH approximation for the spatial gradient of function  $f(\mathbf{x})$  can be obtained by taking derivative of Eq. (33) and considering the fact that  $\nabla f = \nabla f_i - f_i(\nabla 1)$ , which leads to the following equation:

$$\nabla f(\mathbf{x}_i) = \nabla f_i \approx \sum_{j=1}^N V_j (f_j - f_i) \nabla_i W(\mathbf{x}_i - \mathbf{x}_j, \hbar_{sml}) \quad (35)$$

Eq. (35) ensures the vanishing of the gradient of a constant field function. However, it does not always guarantee sufficient accuracy for the approximation, especially when the particle distribution becomes disordered or when particles are close to solid boundaries. A simple approach to address this issue is to normalise the kernel derivative, which leads to the following equation [77,78]

$$\tilde{\nabla} f_i \approx \sum_{j=1}^N V_j (f_j - f_i) \tilde{\nabla}_i W_{ij} \quad \text{and} \quad \tilde{\nabla}_i W_{ij} = \mathbf{L}_{ij} \cdot \nabla_i W_{ij} \quad (36)$$

where  $\mathbf{L}_{ij} = \left[ \sum_{j=1}^N V_j (x_j - x_i)^m \nabla^n_i W_{ij} \right]^{-1}$  is a normalised matrix, and  $m$  and  $n$  indicate coordinate direction with repeated indices implying summation. Eq. (36) yields a second-order accuracy for the SPH approximation of  $\nabla f_i$  and is therefore adopted in this paper to estimate the seepage velocity, which will be discussed in the next section.

On the other hand, to solve the transient seepage flow equation described in the earlier section, one would need an SPH approximation for second-order derivatives. Within the SPH context, there exists an SPH approximation for the Laplacian operator of a scalar quantity, which was originally derived by Brookshaw [58] and was successfully used by Cleary & Monaghan [59,60] to simulate heat conduction problems. This standard SPH formulation of the Laplacian operator was obtained by applying the Taylor series to expand the  $f_j$  around  $\mathbf{x}_i$  up to the third of the accuracy, leading to the following equation:

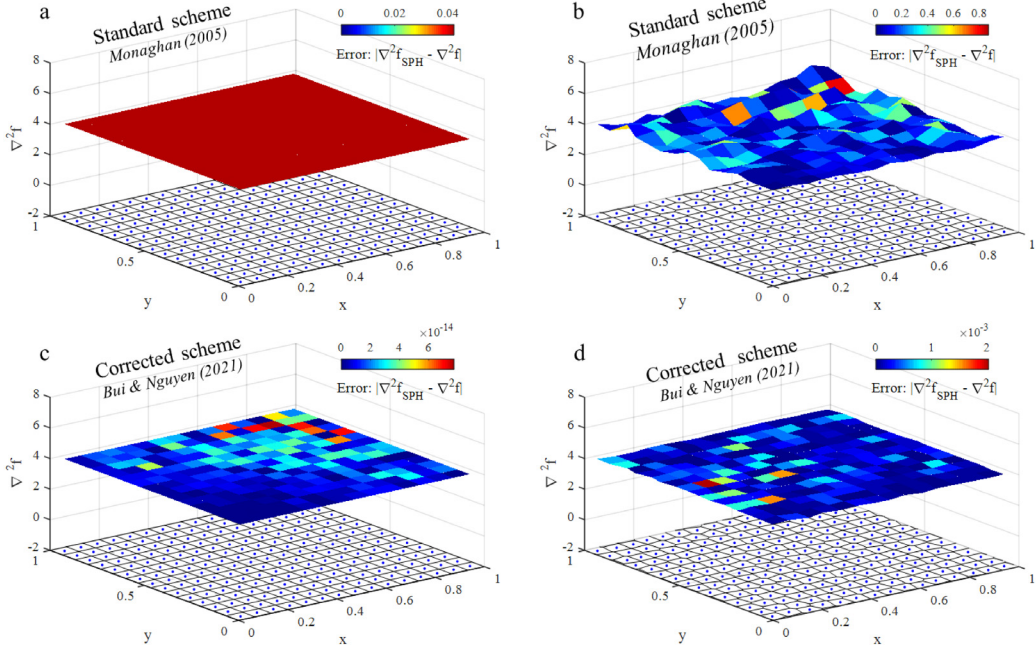


**Fig. 3.** Error analysis on the SPH approximation for the Laplacian of a non-linear function  $f = x^2 + y^2$  on uniform and non-uniform particle systems using SPH schemes presented in [59,65]. Extra layers of SPH particles were created around the boundary to remove the kernel truncation errors.

$$\nabla^2 f_i \approx 2 \sum_{j=1}^N V_j (f_j - f_i) \hat{F}_{ij} \quad \text{with} \quad \hat{F}_{ij} = \frac{\mathbf{r}_{ji} \cdot \nabla_i W_{ij}}{|\mathbf{r}_{ji}|^2} \quad (37)$$

where  $\hat{F}_{ij}$  is a scalar related to the kernel gradient term, with  $\mathbf{r}_{ji} = \mathbf{x}_j - \mathbf{x}_i$ .

Eq. (37) is perhaps the most commonly used SPH operator to solve partial differential equations involving Laplacian operators. One of the key advantages of this formulation is that it only involves the first derivative of the kernel function, thus it is rather simple to compute and could avoid all issues associated with the second derivative of the kernel function, which is highly sensitive to particle distortion [60,65]. Nevertheless, the accuracy of the above SPH Laplacian approximation heavily relies on the accuracy of SPH approximations for the following terms,  $\sum_{j=1}^N V_j r_{ji}^m \hat{F}_{ij} \approx 0$  and  $\sum_{j=1}^N V_j r_{ji}^m r_{ji}^n \hat{F}_{ij} \approx \delta^{mn}$ , which are hardly achieved in SPH, especially when the particle becomes highly disordered or are close to the boundary. To address this issue, Bui and Nguyen [65] recently proposed an improved SPH formulation to approximate the Laplacian operator by directly eliminating the above error-source terms from the consideration of the Taylor expansion series, which leads to the following corrected form of the SPH Laplacian approximation:

$$\tilde{\nabla}^2 f_i = \frac{2}{\mathbf{K}_{ij}^{\text{norm}}} \left[ \sum_{j=1}^N V_j (f_j - f_i) \hat{F}_{ij} - \tilde{\nabla} f_i \sum_{j=1}^N V_j r_{ji}^m \hat{F}_{ij} \right] \quad (38)$$

where  $\mathbf{K}_{ij}^{\text{norm}} = \frac{1}{2} \sum_{j=1}^N V_j (x_{ji}^2 + y_{ji}^2) \hat{F}_{ij}$  is the symmetrised normalisation term and the first derivative  $\tilde{\nabla} f_i$  in Eq. (38) was calculated using Eq. (36). The readers should have immediately seen that, for a uniform distribution of particles, the second term on the right-hand side in Eq. (38) vanishes and  $\mathbf{K}_{ij}^{\text{norm}}$  equals unity. Thus, Eq. (38) reduces to the standard SPH Laplacian approximation in Eq. (37).

The accuracy of the above SPH approximation formula, i.e. Eqs. (37) and (38), for the Laplacian of a non-linear function ( $f = x^2 + y^2$ ) is evaluated and shown in Fig. 3. The approximations were performed on both uniform and non-uniform particle system. The Cubic Spline kernel was adopted with a smoothing length of  $\hbar_{\text{sml}} = 1.3dx$ . In addition, three layer of virtual particle were generated on the boundary domain (not shown in the figure) to avoid the

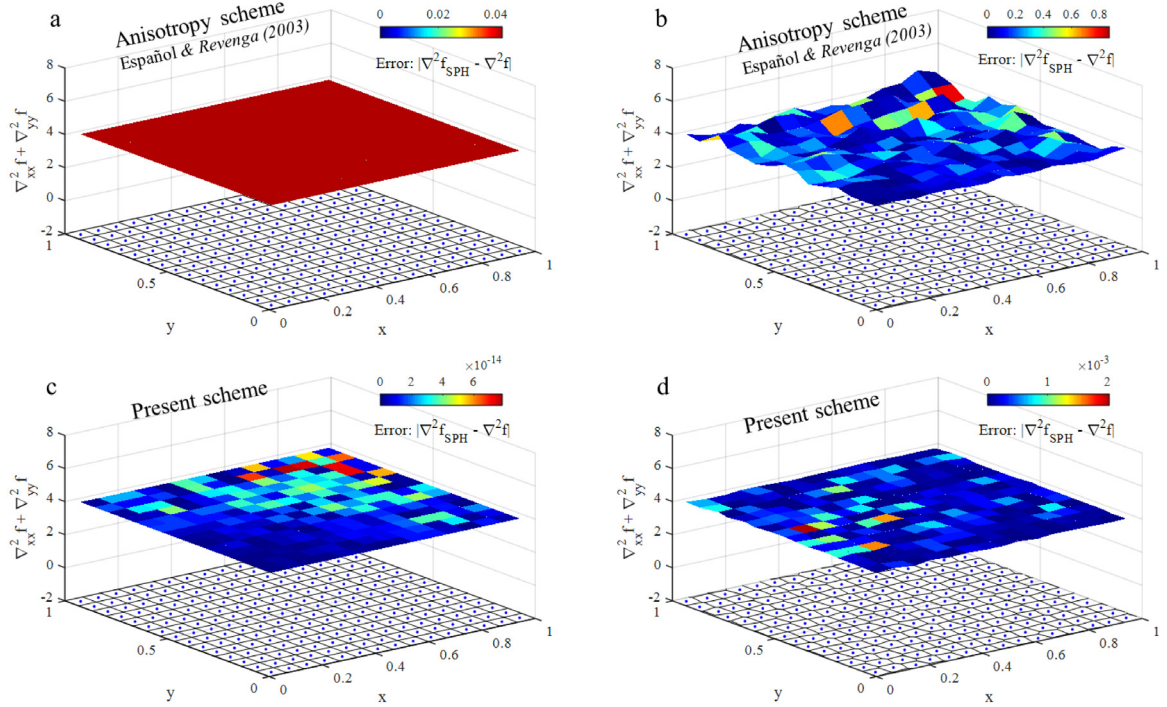


**Fig. 4.** Error analysis on the second derivatives ( $\nabla^2 f = (\nabla_{xx}^2 f) + (\nabla_{yy}^2 f)$ ) of the non-linear function  $f = x^2 + y^2$  calculated on the uniform and non-uniform particle systems.

obvious kernel truncation issue at the boundary. It can be seen that Eq. (37) produces minor errors on the uniform particle system (Fig. 3a), but increases by nearly one orders of magnitude and showing significant fluctuations on the non-uniform particle (Fig. 3b). Clearly, Eq. (37) is still sensitive to the disordered particles, though it is less severe than the SPH Laplacian operator, which makes use of the second derivatives of the kernel function. On the other hand, the improved SPH Laplacian scheme proposed by Bui & Nguyen [65], i.e. Eq. (38), exactly reproduces the theoretical solution for the second derivative of the non-linear function on the uniform particle system (see Fig. 3c). On the non-uniform particle system, Eq. (38) considerably improves the accuracy of Eq. (37). The errors produced by Eq. (38) reduce by two orders of magnitude as compared to those predicted by Eq. (37) and are negligible (see Fig. 3d). Furthermore, Eq. (38) is free from the particle-disordered issue and produced smooth results across the approximation domain.

The above tests suggest that there exists a high-order accurate SPH formulation for approximation of the Laplacian, i.e. (Eq. (38)), which is sufficient for solving isotropic diffusion problems such as heat conduction and seepage flow problems. However, this SPH operator for the Laplacian could not be used to solve diffusion problems involving anisotropic flows due to permeability anisotropy, thus cannot be used to solve unsaturated seepage flow problems through anisotropic porous media. To address this problem, a general SPH operator proposed by Español & Revenga [61] can be adopted and takes the following form:

$$\frac{\partial^2 f_i}{\partial x^m \partial x^n} = \sum_{j=1}^N (f_j - f_i) \left( 4 \frac{r_{ji}^m r_{ji}^n}{|\mathbf{r}_{ji}|^2} - \delta^{mn} \right) \hat{F}_{ij} \quad (39)$$

Different from Eqs. (37) and (38), the above equation involves the second-order spatial gradient with respect to independent coordinates. Therefore, it can be used for solving general diffusion problems involving anisotropic flows, which require the computation of  $\partial^2 f_i / \partial x^2$  and  $\partial^2 f_i / \partial y^2$ , separately. Unfortunately, Eq. (39) shares the same limitation to that of the standard SPH formulation Eq. (37), and thus suffers from low accuracy besides being sensitive to disordered particles (see Fig. 4a and b). For this reason, an improved SPH scheme for the general

approximation of second-order derivatives considering anisotropy diffusions is required, and this is proposed in the next section.

### 3.2. Improved SPH approximation for the second-order derivatives considering anisotropy diffusion

As discussed in the above section, the existing SPH approximation for the second gradient considering anisotropic diffusion shares the same limitation as that of Eq. (37) and thus producing poor performance on the non-uniform particle system. To address this problem, it is important to revisit the sources of those errors. Let us start by considering the Taylor series expansion of a function  $f_j$  around  $\mathbf{x}_i$  up to the second-order accuracy, leading to:

$$f_j = f_i + \frac{\partial f_i}{\partial r^m} r_{ji}^m + \frac{1}{2} \frac{\partial^2 f_i}{\partial r^m \partial r^n} r_{ji}^m r_{ji}^n + O(h^2) \quad (40)$$

Multiplying both sides of the above equation with  $\frac{r_{ji}^m r_{ji}^n}{|\mathbf{r}_{ji}|^2} \tilde{F}_{ij}$ , where  $\tilde{F}_{ij} = \frac{\mathbf{r}_{ji}}{|\mathbf{r}_{ji}|^2} \cdot \tilde{\nabla}_i W_{ij}$  is the scalar part of the normalised kernel gradient and, taking the integral of the resulting equation, yields:

$$\begin{aligned} & \int (f_j - f_i) \frac{r_{ji}^m r_{ji}^n}{|\mathbf{r}_{ji}|^2} \tilde{F}_{ij} d\mathbf{r}_j \\ &= \underbrace{\frac{\partial f_i}{\partial r^{m'}} \int \frac{r_{ji}^{m'} r_{ji}^m r_{ji}^n}{|\mathbf{r}_{ji}|^2} \tilde{F}_{ij} d\mathbf{r}_j}_{\hat{E}^{mm'}} + \underbrace{\frac{1}{2} \frac{\partial^2 f_i}{\partial r^{m'} \partial r^{n'}} \int r_{ji}^{m'} r_{ji}^{n'} \frac{r_{ji}^m r_{ji}^n}{|\mathbf{r}_{ji}|^2} \tilde{F}_{ij} d\mathbf{r}_j}_{\hat{N}^{mm'n'}} \end{aligned} \quad (41)$$

The rearrangement of the above equation leads to the following linear system of equations, which can be solved for the second derivatives of  $f_i$ :

$$\int (f_j - f_i) \frac{r_{ji}^m r_{ji}^n}{|\mathbf{r}_{ji}|^2} \tilde{F}_{ij} dr_j - \frac{\partial f_i}{\partial r^{\alpha'}} \hat{E}^{mm'} = \frac{1}{2} \frac{\partial^2 f_i}{\partial r^{m'} \partial r^{n'}} \hat{N}^{mm'n'} \quad (42)$$

where both  $\hat{E}$  and  $\hat{N}$  are explicitly defined and are computable by SPH. It is noted here that the approach to solving the above linear system equation (Eq. (42)) for the second derivatives of  $f_i$  is similar to the corrective smooth particle hydrodynamics (CSPH) method, originally proposed by Chen et al. [64,79]. However, in contrast to CSPH, Eq. (42) does not involve the second derivative of the kernel function, and thus in principle, is less sensitive to the disorder of SPH particles. In this paper, we will not explore this option because, although it offers a rigorous approach to derive new SPH formulations, it produces cumbersome SPH approximations for the second derivatives that are not very useful for practical applications. Instead, we are interested in a simplified approach that could produce robust SPH formulations with acceptable accuracy.

To establish robust SPH formulations for the second derivatives, let us first consider the fourth-order tensor  $\hat{N}^{\alpha\beta\alpha'\beta'}$  in Eq. (42). Under 2D conditions and symmetric coordinates, the only surviving components take the following forms:

$$A = \int r_{ji}^m r_{ji}^m r_{ji}^m \frac{r_{ji}^m}{|\mathbf{r}_{ji}|^2} \tilde{F}_{ij} d\mathbf{r}_j = \frac{3}{4} \quad (43)$$

$$B = \int r_{ji}^m r_{ji}^m r_{ji}^n \frac{r_{ji}^n}{|\mathbf{r}_{ji}|^2} \tilde{F}_{ij} d\mathbf{r}_j = \frac{1}{4} \quad (44)$$

Making use of Eqs. (43) and (44), Eq. (42) can be further expanded with respect to free indexes, leading to the following equations:

$$\int (f_j - f_i) \frac{x_{ji} x_{ji}}{|\mathbf{r}_{ji}|^2} \tilde{F}_{ij} dr_j - \frac{\partial f_i}{\partial r^{\alpha'}} \hat{E}^{xx\alpha'} = \frac{1}{2} (A - B) \frac{\partial^2 f_i}{\partial x^2} + \frac{1}{2} B \nabla^2 f \quad (45)$$

$$\int (f_j - f_i) \frac{y_{ji} y_{ji}}{|\mathbf{r}_{ji}|^2} \tilde{F}_{ij} dr_j - \frac{\partial f_i}{\partial r^{\alpha'}} \hat{E}^{yy\alpha'} = \frac{1}{2} (A - B) \frac{\partial^2 f_i}{\partial y^2} + \frac{1}{2} B \nabla^2 f \quad (46)$$

$$\int (f_j - f_i) \frac{x_{ji} y_{ji}}{|\mathbf{r}_{ji}|^2} \tilde{F}_{ij} dr_j - \frac{\partial f_i}{\partial r^{\alpha'}} \hat{E}^{xy\alpha'} = B \frac{\partial^2 f_i}{\partial x \partial y} \quad (47)$$

At this point, the readers could immediately see that the summation of Eqs. (45) and (46) yields the following SPH approximation for the Laplacian, which shares a similar form (though not exactly the same) that proposed by Bui and Nguyen [65]:

$$\nabla^2 f_i = \frac{2}{A + B} \left[ \int (f_j - f_i) \tilde{F}_{ij} dr_j - \frac{\partial f_i}{\partial r^{\alpha'}} (\hat{E}^{xxm'} + \hat{E}^{yym'}) \right] \quad (48)$$

Finally, by substituting Eq. (48) into Eqs. (45) and (46) with  $A$  and  $B$  explicitly defined in Eqs. (43) and (44), and converting integrals to summations, the following SPH approximations for the second derivatives of  $f_i$  with respect to  $x$  and  $y$ , can be derived:

$$\frac{\partial^2 f_i}{\partial x^2} = \sum_{j=1}^N V_j (f_j - f_i) \left( 4 \frac{x_{ji} x_{ji}}{|\mathbf{r}_{ji}|^2} - 1 \right) \tilde{F}_{ij} dr_j + \frac{\partial f_i}{\partial r^{m'}} \sum_{j=1}^N V_j r_{ij}^{m'} \left( \frac{y_{ji} y_{ji}}{|\mathbf{r}_{ji}|^2} - 3 \frac{x_{ji} x_{ji}}{|\mathbf{r}_{ji}|^2} \right) \tilde{F}_{ij} \quad (49)$$

$$\frac{\partial^2 f_i}{\partial y^2} = \sum_{j=1}^N V_j (f_j - f_i) \left( 4 \frac{y_{ji} y_{ji}}{|\mathbf{r}_{ji}|^2} - 1 \right) \tilde{F}_{ij} dr_j + \frac{\partial f_i}{\partial r^{m'}} \sum_{j=1}^N V_j r_{ij}^{m'} \left( \frac{x_{ji} x_{ji}}{|\mathbf{r}_{ji}|^2} - 3 \frac{y_{ji} y_{ji}}{|\mathbf{r}_{ji}|^2} \right) \tilde{F}_{ij} \quad (50)$$

$$\frac{\partial^2 f_i}{\partial x \partial y} = \sum_{j=1}^N V_j (f_j - f_i) 4 \frac{x_{ji} y_{ji}}{|\mathbf{r}_{ji}|^2} \tilde{F}_{ij} dr_j - \frac{\partial f_i}{\partial r^{m'}} \sum_{j=1}^N V_j r_{ij}^{m'} \frac{4 x_{ji} y_{ji}}{|\mathbf{r}_{ji}|^2} \tilde{F}_{ij} \quad (51)$$

where the first derivative  $\partial f_i / \partial r^{m'}$  is computed using Eq. (36). The above SPH approximations for the second derivatives can be recast in the following index form for general usage:

$$\frac{\partial^2 f_i}{\partial x^m \partial x^n} = \sum_{j=1}^N V_j (f_j - f_i) \mathcal{D}^{mn} \tilde{F}_{ij} - \frac{\partial f_i}{\partial r^{m'}} \sum_{j=1}^N V_j r_{ji}^{m'} \mathcal{D}^{mn} \tilde{F}_{ij} \quad (52)$$

where  $\mathcal{D}^{mn} = 4 \frac{r_{ji}^m r_{ji}^n}{|\mathbf{r}_{ji}|^2} - \delta^{mn}$ , with  $\delta^{mn}$  being the Kronecker delta, and  $m$  and  $n$  indicating coordinate directions.

It can be seen from the newly derived SPH formulation that the first term on the right-hand side of this equation shares a similar form to the formulation derived Español & Revenga [61], which is commonly used in literature for solving anisotropic diffusion problems. However, it is noted here that the formulation proposed by Español & Revenga [61] used less accurate formulations to compute  $\tilde{F}_{ij}$  and thus is less accurate than the first term on the right-hand side of Eq. (52). Furthermore, the SPH formulation derived by Español & Revenga [61], and all existing SPH formulations for the second derivatives that make use of their approach, does not contain the second term on the right-hand side of Eq. (52), which is the key factor to produce accurate SPH approximations for the second derivatives. The readers should have noticed that this term represents the source of errors associated with the first derivative of  $f_i$  from the Taylor expansion series, and the subtraction of this term from Eq. (52) helps to completely remove this error source. For an ideal spherical coordinate system, this term vanishes and thus Eq. (52) returns to the original SPH approximation form for the second derivatives derived by Español & Revenga [61].

To demonstrate the effectiveness and accuracy of the newly proposed SPH formulation, let us apply this formulation to evaluate the value of a non-linear function ( $f = x^2 + y^2$ ) on both uniform and non-uniform particle systems, and comparing its performances against theoretical results as well as those predicted by the original formulation proposed by Español & Revenga [61]. Similar to the previous tests, the Cubic Spline kernel with a smoothing length of  $\hbar_{sm} = 1.3dx$  was adopted. Fig. 4 shows the performance of the newly proposed SPH formulation for the second derivatives considering anisotropy, i.e., Eq. (52). It can be seen that the SPH formulation proposed by Español & Revenga [61] produces a small error ( $\sim 1\%$ ) for the approximation of the Laplacian of  $f$  (i.e.  $\langle \nabla^2 f \rangle = \nabla_{xx}^2 f + \nabla_{yy}^2 f$ ) on the regular particle system (see Fig. 4a), while this error increases by an order of magnitude ( $> 20\%$ ) on the non-regular particle configuration or when particles become heavily disorder (see Fig. 4b). These results also indicate that the SPH formulation proposed by Español & Revenga [61] shares the same level of accuracy as the standard SPH approximation for the Laplacian in Eq. (37). On the other hand, the newly proposed SPH formulation, Eq. (52), exactly reproduces analytical results on the regular particle system, as shown in Fig. 4c. It is worth pointing out here that the error bar of magnitude  $10^{-14}$  included in this figure simply indicates

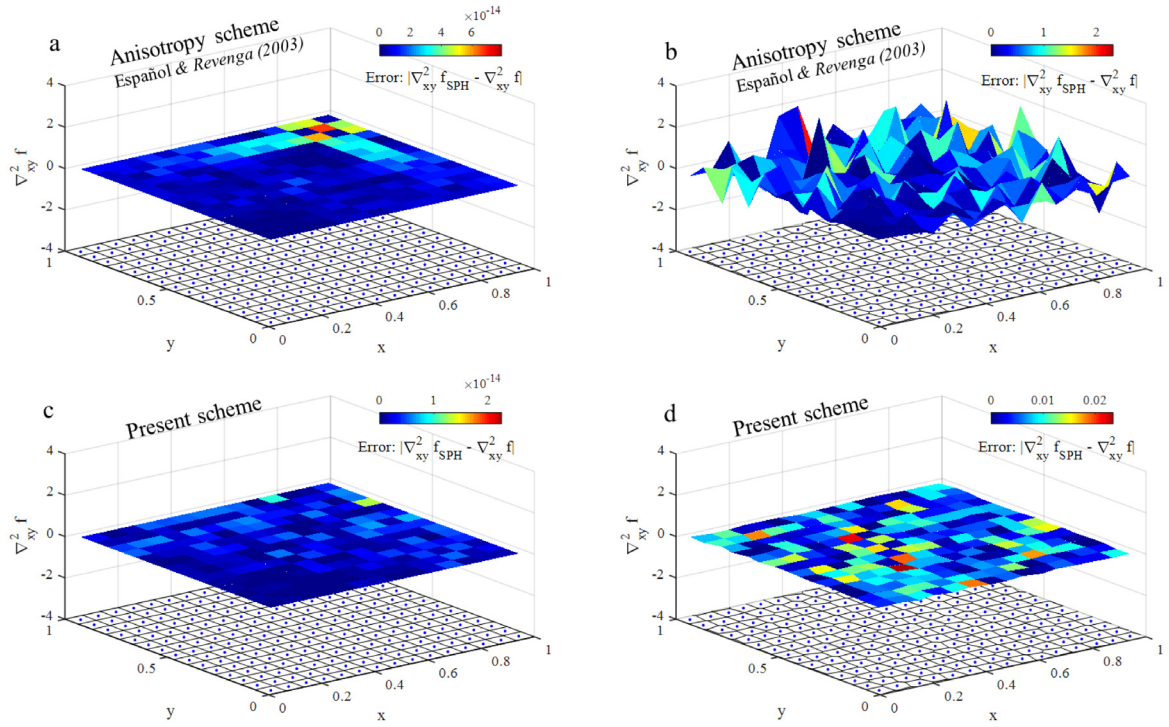


**Fig. 5.** Error analysis on the second-order mixed derivatives ( $\partial^2 f / \partial x \partial y$ ) of the non-linear function  $f = x^2 + y^2$  calculated on the uniform and non-uniform particle system.

the round-off error produced by the computer software. More importantly, the newly proposed SPH formulation considerably improves the accuracy of SPH approximation for the Laplacian of  $f$  on the irregular particle system with more and less the same computational cost, as shown in Fig. 4d, with the maximum error reducing by four orders of magnitude, and achieves the same level of accuracy to that obtained by the SPH Laplacian formulation, Eq. (38), which was recently proposed by Bui and Nguyen (2021) [65]. Note that Eq. (38) computes the entire Laplacian approximation ( $\langle \nabla^2 f \rangle$ ) in one go, while Eq. (52) computes each component of the Laplacian (i.e.  $\langle \nabla_{xx}^2 f \rangle$  and  $\langle \nabla_{yy}^2 f \rangle$ ) and then adding them together (i.e.  $\langle \nabla^2 f \rangle = \langle \nabla_{xx}^2 f + \nabla_{yy}^2 f \rangle$ ). For this reason, Eq. (52) is general and thus can be used to solve anisotropic diffusion problems. Finally, one may wish to see if the newly proposed SPH formulation could accurately reproduce the approximation for the mixed second derivative of function  $f$ , i.e.  $\langle \nabla_{xy}^2 f \rangle$  or  $\partial^2 f / \partial x \partial y$ . The results of this approximation on the regular and non-regular particle systems are shown in Fig. 5, as compared to those predicted by the original formulation proposed by Espanol & Revenga [61]. It can be seen again that the newly proposed SPH formulation exactly reproduces analytical results on the regular particle system and produce acceptable results on the non-regular particle system with the maximum error of less than 2% (Fig. 5d). In contrast, the formulation proposed by Espanol & Revenga [61] produce insignificant errors on the uniform particle system (Fig. 5a), but this error increases by several orders of magnitude on the irregular particle configuration (Fig. 5b). Furthermore, the formulation proposed by Espanol & Revenga is shown to be highly sensitive to disordered particles. Therefore, it can be concluded that the newly developed SPH formulation for the approximations of second derivatives considering the anisotropy proposed in this paper is robust and more accurate. It outperforms existing SPH formulations in literature, especially when being used on non-uniform particle systems or for cases where particles are highly disordered, while sharing similar computational costs. This newly developed SPH formulation is now ready to be used to predict complex diffusion problems involving anisotropic flows. In the next section, this new formulation will be used to solve unsaturated transient seepage flows in anisotropic porous media.

### 3.3. SPH approximations of transient unsaturated seepage flow through anisotropic porous media

As established in the earlier section, the transient behaviour of unsaturated/saturated seepage flows through anisotropic porous media can be described by Eq. (29). To solve this equation within the SPH framework, one needs to convert this equation into the ordinary differential equation and this will be elucidated in this section. Let us first recall Eq. (29), which can be rewritten as follows:

$$\frac{dh}{dt} = \frac{1}{\tilde{C}_{Sr}} \nabla \cdot [\mathbf{k} \nabla (h + z)] \quad (53)$$

where  $\mathbf{k}$  is the anisotropic water permeability tensor.

To approximate the right-hand side of Eq. (53) in SPH, one needs to recast this equation to obtain a consistent SPH approximation form for the second derivative of a function, i.e. Eq. (52). This can be achieved by adopting the following transformation to the right-hand side of Eq. (53):

$$\nabla \cdot (\mathbf{k} \nabla H) = \frac{1}{2} [\nabla^2 (\mathbf{k} H) + \mathbf{k} \cdot \nabla^2 H - H \nabla^2 \mathbf{k}] \quad (54)$$

The SPH approximation for the second derivative of a function, i.e. Eq. (52), can be now used to evaluate the value of each component on the right-hand side in Eq. (54) at a particle  $i$ , leading to:

$$\begin{aligned} \nabla^2 (\mathbf{k} H)|_i &= \sum_{j=1}^N V_j (k_j^{mn} H^j - k_i^{mn} H^i) \mathcal{D}^{mn} \tilde{F}_{ij} - \frac{\partial(k_i^{mn} H^i)}{\partial r^{m'}} \sum_{j=1}^N V_j r_{ji}^{m'} \mathcal{D}^{mn} \tilde{F}_{ij} \\ \mathbf{k} \cdot \nabla^2 H|_i &= k_i^{mn} \sum_{j=1}^N V_j (H^j - H^i) \mathcal{D}^{mn} \tilde{F}_{ij} - k_i^{mn} \frac{\partial H_i}{\partial r^{m'}} \sum_{j=1}^N V_j r_{ji}^{m'} \mathcal{D}^{mn} \tilde{F}_{ij} \\ H \nabla^2 \mathbf{k}|_i &= H^i \sum_{j=1}^N V_j (k_j^{mn} - k_i^{mn}) \mathcal{D}^{mn} \tilde{F}_{ij} - H^i \frac{\partial k_i^{mn}}{\partial r^{m'}} \sum_{j=1}^N V_j r_{ji}^{m'} \mathcal{D}^{mn} \tilde{F}_{ij} \end{aligned} \quad (55)$$

where the super- and subscripts  $i$  and  $j$  are equally used to refer to SPH particles. Finally, by substituting Eq. (55) into Eq. (54) and rearranging the resulting equation for a particle  $i$ , the following SPH approximation equation can be obtained:

$$\frac{dh}{dt} = \frac{1}{\tilde{C}_{Sr}} \left\{ \sum_{j=1}^N V_j \bar{k}_{ij}^{mn} (H^j - H^i) \mathcal{D}^{mn} \tilde{F}_{ij} - k_i^{mn} \frac{\partial H_i}{\partial r^{m'}} \sum_{j=1}^N V_j r_{ji}^{m'} \mathcal{D}^{mn} \tilde{F}_{ij} \right\} \quad (56)$$

where  $\bar{k}_{ij}^{mn} = (k_i^{mn} + k_j^{mn})/2$  is the arithmetically mean value of the water permeability and the first derivative term  $\frac{\partial H_i}{\partial r^{m'}}$  can be calculated using Eq. (36). A consistent SPH equation for solving the water pressure head can be obtained by replacing  $H$  by  $(h + z)$ , giving:

$$\frac{dh^i}{dt} = \frac{1}{\tilde{C}_{Sr}} \left\{ \sum_{j=1}^N V_j \bar{k}_{ij}^{mn} [(h^j + z^j) - (h^i + z^i)] \mathcal{D}^{mn} \tilde{F}_{ij} - k_i^{mn} \frac{\partial H_i}{\partial r^{m'}} \sum_{j=1}^N V_j r_{ji}^{m'} \mathcal{D}^{mn} \tilde{F}_{ij} \right\} \quad (57)$$

It is noticed from the above equation that the SPH approximation of the unsaturated seepage flow equation automatically results in the mean average of the water permeabilities  $k_i^{mn}$  and  $k_j^{mn}$  (i.e. arithmetically mean  $\bar{k}_{ij}^{mn} = (k_i^{mn} + k_j^{mn})/2$ ) when a pair of particles are involved in the SPH summation. This guarantees the balance of mass exchange between two particles  $i$  and  $j$  when the water flux transfers from particle  $i$  with a higher hydraulic head to particle  $j$  with a lower hydraulic head. An alternative to the arithmetic mean of water permeability ( $\bar{k}_{ij}^{mn}$ )

in Eq. (57) is the harmonic mean of  $\bar{k}_{ij}^{mn} = \frac{2k_i^{mn}k_j^{mn}}{(k_i^{mn}+k_j^{mn})}$ , which was commonly used in the literature for solving isotropic heat conduction problems using the standard SPH approximation for Laplacian [59,60] and yielded good results. However, unlike the heat conduction problems, the harmonic mean of water permeability produces incorrect results when being used to solve 1D unsaturated seepage flow problems. Furthermore, it causes fluctuations in

the PWP close to the seepage wetting front for anisotropic seepage flows. Therefore it is not recommended for solving transient seepage flow in anisotropic porous media. On the other hand, the arithmetically mean performs well, including the disjoining region where the water permeability is discontinuous (see Section 5.3), and hence is recommended and adopted in this paper. Finally, once the evolution of unsaturated seepage flows is solved, one may wish to calculate the specific discharge of water flow  $\mathbf{q} = \mathbf{k}\nabla(h + z)$ , which involves the first derivative of the total head ( $h + z$ ). A direct approach that makes use of the SPH gradient estimator, i.e. Eq. (36), to evaluate the specific discharge of water flow at a particle  $i$  results in the following equation:

$$\mathbf{q}_i = \mathbf{k} \sum_{j=1}^N V_j [(h^j + z^j) - (h^i + z^i)] \tilde{\nabla}_i W_{ij} \quad (58)$$

It is noted that Eq. (58) violates the mass conservation law when the water flux flows from particle  $i$  to particle  $j$  because  $\mathbf{q}_i \neq \mathbf{q}_j$  for a nonhomogeneous porous system (i.e.  $\mathbf{k}^i \neq \mathbf{k}^j$ ). To avoid this problem, one can recast the formulation of the specific discharge as follows:

$$\mathbf{q} = \mathbf{k}\nabla(h + z) = \mathbf{k}\nabla H = \frac{1}{2} [\nabla(\mathbf{k}H) + \mathbf{k}\nabla H - H\nabla\mathbf{k}] \quad (59)$$

Applying the SPH gradient estimator, i.e. Eq. (36), to evaluate the gradient term of the above equation and rearranging the resulting equation, the specific discharge of water flow at a particle  $i$  can be computed by the following equation:

$$\mathbf{q}_i = \sum_{j=1}^N V_j \bar{\mathbf{k}}^{ij} [(h^j + z^j) - (h^i + z^i)] \tilde{\nabla}_i W_{ij} \quad (60)$$

which guarantees the balance of water flux between two particles  $i$  and  $j$ .

### 3.4. Spatial discretisation in SPH - Weighted Voronoi Tessellations

Spatial discretisation is the next step required in SPH to solve an unsaturated seepage flow problem after establishing its governing equations. It is considered as one of the most important topics of SPH that requires further attention to make the method more suitable for large scale engineering applications. In the standard SPH method, the spatial discretisation of a continuum domain (e.g. an unsaturated porous medium) is obtained by placing particles in a regular cubic lattice, as shown in Fig. 6a. Each SPH particle then occupies the same initial continuum, which can be either remained unchanged or updated during the computational process. These particles can move freely in the computational space and carrying field variables of the corresponding continuum space they occupied (e.g. the pressure head or seepage velocity). So far, this regular cubic configuration has been the most popular in SPH applications owing to its simplicity and capability to produce highly accurate SPH approximation results. For unsaturated seepage flow problems, this simple configuration also helps to achieve highly accurate results, but becoming less efficient and requiring high computational costs for large-scale applications, where variable resolutions of spatial discretisation are more suitable. In this paper, a variable resolution weighted Voronoi tessellation is adopted to facilitate the application of the proposed unsaturated seepage flow SPH model for large scale applications. Along with this, we will also demonstrate that our proposed SPH framework for solving unsaturated seepage flow problems could yield not only highly accurate results on the regular cubic particle configuration (Fig. 6a) but also the same level of accuracy on the weighted Voronoi particle configuration, as shown in Fig. 6b, thanks to the newly developed SPH formulations for the second derivatives.

One of the key requirements to produce an optimal Voronoi tessellation particle configuration for SPH simulations is that of the volume of each Voronoi particle  $V_j$  must not be significantly different from its neighbours, and changes in the size of Voronoi particles (or Voronoi volumes) need to occur gradually in all directions. To obtain such a Voronoi tessellation configuration suitable for SPH applications, a weighted Voronoi tessellation (WVT) technique [80,81] that makes use of Lloyd's algorithm [82] to optimise the Voronoi volume is adopted in this paper. Fig. 7 shows the process of how to achieve a regular Voronoi particle system based on the WVT. First, a set of random points  $\mathbf{x}_{j(t0)}$  are created and randomly distributed within the computation domain, through which highly random Voronoi volumes (particles) can be generated, each of which possesses a volume  $V_{j(t0)}$  and their own vertexes  $\mathbf{x}_{v_j}$  (Fig. 7a). The centre of each Voronoi can be then located using the coordinate information of

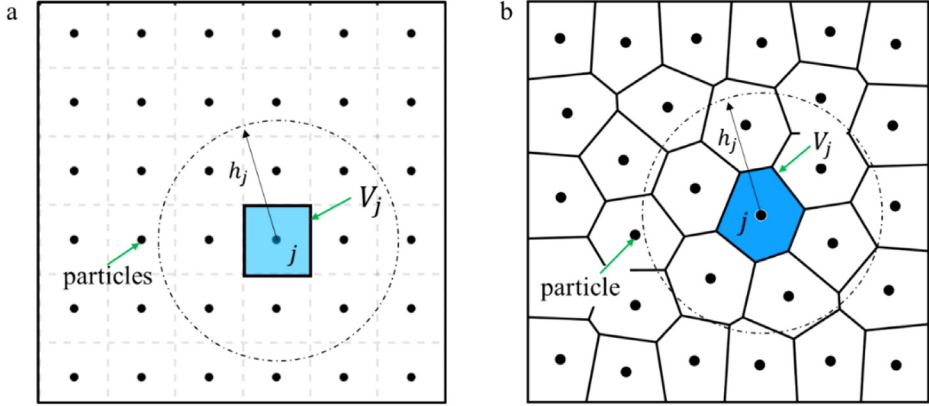


**Fig. 6.** Schematic diagram of two particle systems in SPH (a) the uniform particle system; (b) the random particle system associated with Voronoi cells.

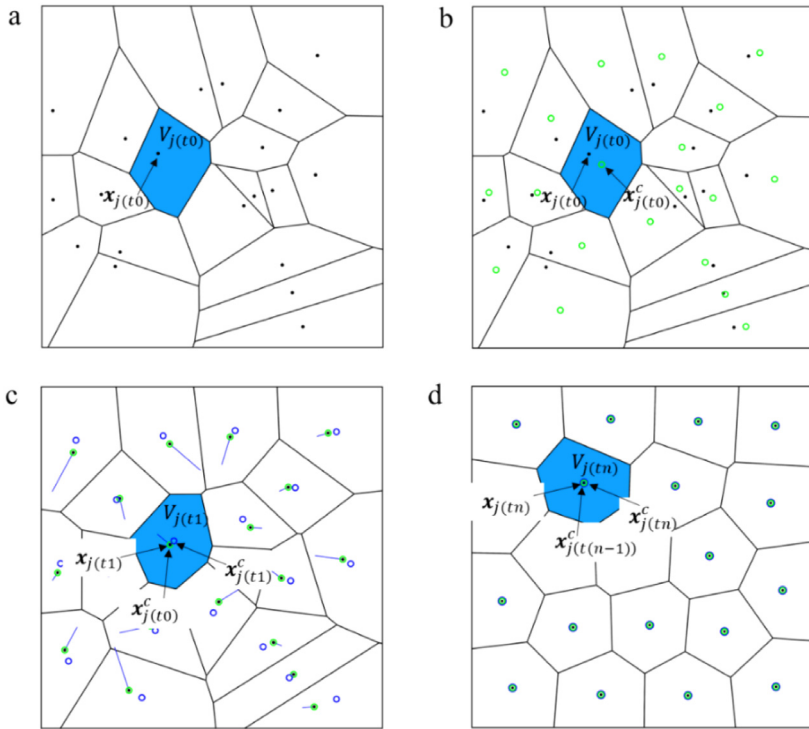


**Fig. 7.** The process to generate a weighted Voronoi particle system suitable for SPH.

Voronoi vertexes  $\mathbf{x}_{j(t0)}^c = \sum \mathbf{x}_{v_j} / N_j$  with  $N_j$  being the number of vertexes of each Voronoi (Fig. 7b). Next, Lloyd's algorithm is applied to optimise the Voronoi volume by replacing  $\mathbf{x}_{j(t0)}$  by  $\mathbf{x}_{j(t0)}^c$  and reconstructing the Voronoi mesh (Fig. 7c). This process is repeated until a certain convergent error is achieved, which results in a uniform Voronoi particle system suitable for SPH applications (Fig. 7d). Finally, the smoothing length required for SPH computation can be estimated by  $h_j^{sm} = 1.3\sqrt{V_{max}}$ , where  $V_{max}$  is the largest area of the Voronoi cells to ensure that the computation of any variables at any particle centre will consider the contributions of all neighbouring particles. The key algorithm to construct the required Voronoi particle configuration is summarised in Table 2, while for the detail theories, we refer readers to the works reported in [68–70,80–82].

**Table 2**

Implementation of Lloyd's algorithm.

<b>Initialisation:</b> $\mathbf{x}_{j(t0)}$ , $\mathbf{V}_{j(t0)}$ , $\varepsilon_{tol}$	% Initialisation of Variables
<b>while</b> $k \leq M$ <b>and</b> $E_r > \varepsilon_{tol}$	% M: the max iteration step
Compute the mesh centre $\mathbf{x}_{j(k)}^c$	% k: the current iteration step
$\mathbf{x}_j^c = \frac{\sum \mathbf{x}_{v_j}}{N_j}$	
Update Voronoi centre	
$\mathbf{x}_{j(k)} \leftarrow \mathbf{x}_{j(k-1)}^c$	
Re-construct Voronoi diagram $\mathbf{V}_{j(k)}$	
Calculate convergence error $E_r$ according to [81]	
$E_r = \frac{N}{ \mathbf{V}_j^{total} ^{1.5}} \left( \sum_{j=1}^N \ \mathbf{V}_j\ ^2 \left  \mathbf{x}_{j(k)} - \mathbf{x}_{j(k)}^c \right ^2 \right)^{0.5} \quad (61)$	
Continue: $k \leftarrow k + 1$	
<b>end while</b>	
<b>Output:</b> $\mathbf{x}_{j(k)}$ , $\mathbf{V}_{j(k)}$	

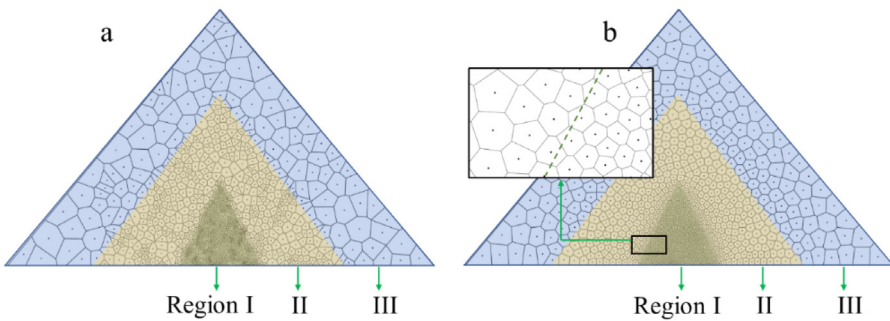


**Fig. 8.** The process to generate a Voronoi particle configuration with multiple resolutions suitable for SPH simulations: (a) Before the optimisation process using the Lloyd Algorithm and (b) After the optimisation process with 15 iteration steps.

To produce a Voronoi discretisation particle configuration with multiple resolutions suitable for SPH simulations, the above WVT algorithm is further extended to force the size of Voronoi particles (or Voronoi volumes) to change gradually in all directions. Fig. 8 outlines the key steps required to achieve a multiple-resolution SPH discretisation domain. Firstly, the triangle domain is divided into three sub-regions, each of which contains a different number of random points, depending on the desired resolution of each region. In this example, the sub-region in the centre of the domain requires higher resolution and thus contains more random points. Next, the Voronoi particle system is constructed (see Fig. 8a) for each sub-region following the same algorithm described in Table 2. To control the size of Voronoi particles in each sub-region, a set of density functions are used and kept unchanged inside their corresponding sub-regions during the optimisation process, i.e. the number of pre-assigned random points remains unchanged in each sub-region [69]. Accordingly, a Voronoi particle system with multiple resolutions could be generated. However, these Voronoi particle systems may not be well suitable for SPH simulations because the size of Voronoi particles at the disjoining boundaries between two sub-regions might be significantly different from others. In this paper, to avoid this problem, a minor modification to the algorithm proposed in [69] is made by removing the density constraint in each sub-region. Accordingly, the pre-assigned random points in each sub-region can travel across disjoining boundaries between two sub-regions. This modification enables producing a Voronoi particle system with particle size gradually changing in all directions across the disjoining boundaries, as shown in Fig. 8b. This smooth transition in the particle volume between sub-regions will help to obtain a continuous distribution of computing field variables between different resolution zones. Again, the same smoothed length estimated from  $\hbar_{smj} = 1.3\sqrt{V_{max}}$ , where  $V_{max}$  is the largest area of the Voronoi cells in each sub-region, thus ensuring that the computation of any variables at any particle centre will consider the contributions of all neighbouring particles. The applications of this spatial discretisation will be discussed in Section 5.5.

### 3.5. Time integration

A suitable time integration scheme is now required to solve the SPH governing equations for unsaturated seepage flows, i.e. Eq. (57) and its counterparts. In this paper, the second-order accurate Leap-Frog (LF) algorithm is adopted due to its well-known low memory storage requirement in the computation process and high efficiency [83]. In the LF algorithm, the state variables are updated at the mid-time step as follows:

$$h_{n+1/2} = h_{n-1/2} + \Delta t \left( \frac{dh}{dt} \right)_n \quad (62)$$

where  $\left( \frac{dh}{dt} \right)_n$  is the rate of change of water pressure head at time ( $t = n$ ). Once the water pressure head at the mid-time step ( $h_{n+1/2}$ ) is determined, its associated state variables including the degree of saturation ( $S^r$ ), water conductivities ( $\mathbf{k}$ ) and the hydraulic head ( $H$ ) are updated as follows:

$$H_{n+1/2} = h_{n+1/2} + \Delta z \quad (63)$$

$$S^r_{n+1/2} = S_{res} + (S_{sat} - S_{res}) [1 + (g_a |h_{n+1/2}|)^{g_n}]^{g_c} \quad (64)$$

$$\mathbf{k}_{n+1/2} = \mathbf{k}^{sat} \cdot S_{n+1/2}^{e_{gl}} \left[ 1 - \left( 1 - S_{n+1/2}^{e_{gl}} \right)^{-g_c} \right]^2 \quad (65)$$

The stability of the above LF time integration scheme is maintained by enforcing the Courant–Friedrichs–Lowy (CFL) condition, which was derived in [Appendix](#). This restricts the size of the time-step to be proportional to the smoothing length, given by:

$$\Delta t \leq CFL \frac{\tilde{C}_{Sr} \hbar_{sml}^2}{k^{sat}} \quad (66)$$

where  $C_{CFL}$  is a constant parameter;  $\tilde{C}_{Sr}$  is the seepage storage term;  $\hbar_{sml}$  is the minimum smoothing length; and  $k^{sat}$  is the saturated seepage permeability. In paper,  $C_{CFL} = 0.1$  was found to be suitable for all applications described in Section 5. It is noted here that  $\tilde{C}_{Sr}$  also changes when the seepage flow moves from unsaturated to saturated flow regimes, and thus the above time step  $\Delta t$  adapts with the flow conditions.

## 4. Boundary conditions for unsaturated seepage flows

The boundary condition is another essential factor that needs to be considered in the numerical solution to seepage problems. In this section, given it is the first to solve saturated/unsaturated seepage flow problems in SPH using a single layer of particle, some commonly encountered boundary conditions (see [Fig. 9](#)) required to solve saturated/unsaturated seepage flow problems are discussed, and the implementation of these boundary conditions in SPH is presented. To facilitate the descriptions, we reserve the subscript  $\Gamma$  for the general boundary domain,  $H|_\Gamma$  for the hydraulic head on  $\Gamma$ ,  $h|_\Gamma$  for the water pressure head on  $\Gamma$ , and  $Q$  for the water flux.

In SPH, the seepage boundary conditions shown in [Fig. 9](#) can be either imposed through boundary particles, which are generated in the boundary domains or directly imposed on SPH particles on particular boundary domains such as on free-surface boundaries. [Fig. 10](#) outlines the key concepts of how required seepage boundary conditions are imposed on SPH particles and the details of these conditions are discussed in the following section for each specific boundary condition.

### a. Prescribed hydraulic head boundary

The hydraulic head boundary is also known as the Dirichlet boundary condition [74], which is one of the simplest and the most encountered boundary conditions required in modelling saturated seepage flow. As shown in [Fig. 9](#), this boundary condition indicates the constant hydraulic head boundary on the upstream and downstream boundaries. In this case, the form of the boundary condition reads:

$$H|_\Gamma = H_u \text{ with } H|_\Gamma = H_d \quad (67)$$

where  $H_u$  and  $H_d$  are constant hydraulic heads describing the groundwater table on the upstream and downstream boundaries, respectively.

In SPH, this type of boundary condition can be either directly imposed on real SPH particles, which are located on free-surface boundaries that satisfies this boundary condition or imposed on boundary particles, which are generated

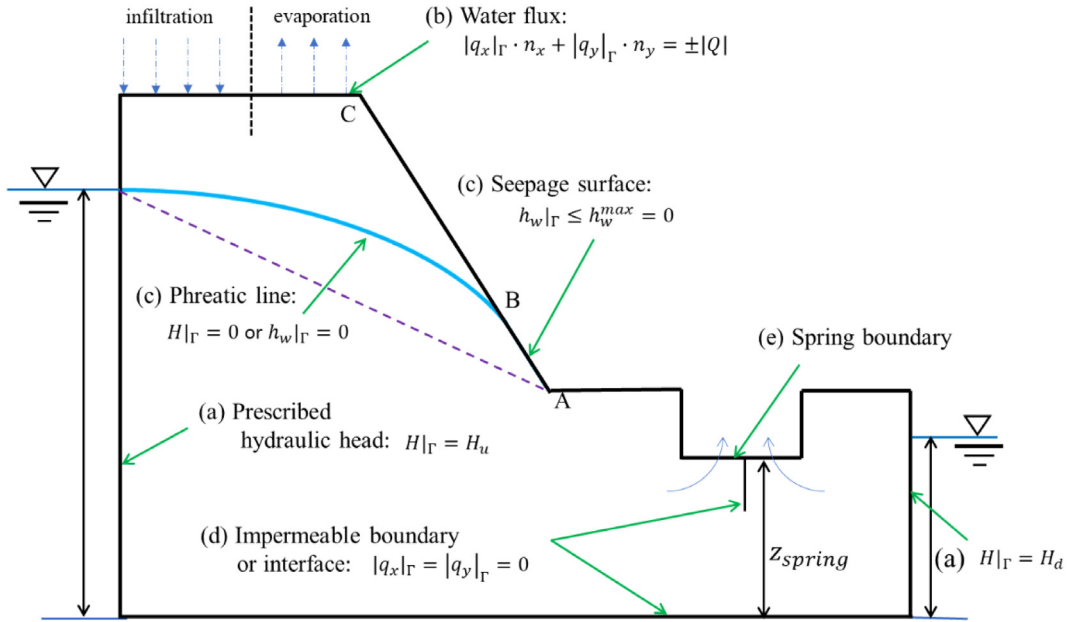


**Fig. 9.** Complex boundary conditions required for numerical solutions of saturated/unsaturated seepage flow in a porous medium.

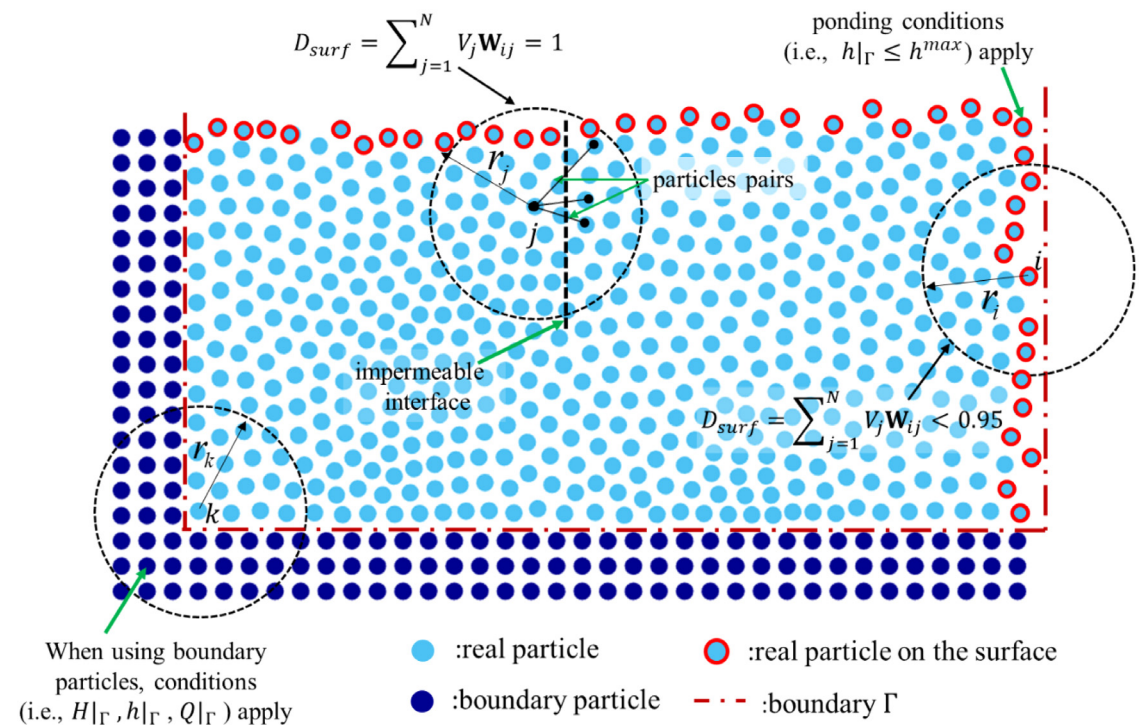


**Fig. 10.** Outline of strategy to impose required boundary conditions for modelling saturated/unsaturated seepage flows into SPH.

on solid boundary regions and often used to represent the solid boundaries when applying SPH to solve general geotechnical problems [32,84]. To directly impose hydraulic head boundary condition on real SPH particles, one needs to identify SPH particles located close to free-surface boundaries and satisfy this boundary condition. Particles close to free-surface boundaries can be identified if the following condition meets:

$$D_{\text{surf}} = \sum_{j=1}^N V_j W_{ij} < 0.95 \quad (68)$$

On the other hand, for the boundary particle approach, depending on the specific kernel function, several layers of boundary particles (three layers for the cubic spline function) are generated in the boundary region. These boundary particles have the same physical properties as real particles but carrying additional information of the prescribed hydraulic head, which is maintained to be constant during the entire computation process. Boundary particles contribute to SPH summations and thus can automatically impose the Dirichlet boundary conditions to the computational domain.

### b. Prescribed water flux boundary

This type of boundary condition is often encountered on the ground surface, such as water flux infiltrating to the soil due to rainfall or evaporation, and is also commonly known as the Neumann boundary condition. In this case, a prescribed water flux takes the form:

$$|q_x|_\Gamma \cdot n_x + |q_y|_\Gamma \cdot n_y = \pm |Q| \quad (69)$$

where  $\mathbf{q} = |Q|$  is the source/sink term with the “+” sign denoting inflow, while the “−” sign indicating outflow (infiltration or evaporation);  $\mathbf{n}$  is the vector normal to the boundary. Note that, for the case of no-flux, the source/sink term equals zero.

In a wetting or drying test, the flux value  $|Q|$  may become time-dependent since the amount of inflow or outflow is determined by the capacity of the soil limits. For instance, when the flux value exceeds the infiltration capacity of the soil, a “ponding” condition of  $H = H_{\max}$  takes place, in which  $H_{\max}$  is defined by the infiltration capacity of soil and can be calibrated using experiments. In such cases, the prescribed flux rate boundary condition will be switched to a prescribed hydraulic head boundary. The same concept can also be applied to the drying test. In SPH, this type of boundary condition can be straightforwardly applied by imposing the prescribed flux value on SPH particles located on free-surface boundaries, which are either known in advance or can be detected by applying Eq. (68) for each computational cycle.

### c. Phreatic line and free-seepage surface

These types of boundary conditions are the most critical to the solutions of seepage problems. The shape of the phreatic line (also known as phreatic surface) usually takes the following form [74]:

$$\Gamma(x, y, t) \equiv h(x, y, t) = H(x, y, t) - z = 0 \quad (70)$$

Eq. (70) indicates that the water pressure on the phreatic line is zero. In addition, when the phreatic line reaches an open downstream boundary (e.g. slope surface AC in Fig. 9), it becomes a seepage surface (e.g. segment AB in Fig. 9). Typically, the location of the phreatic line and seepage surface is unknown prior to the seepage analysis. Thus, a trial approach can be adopted to locate an initial guess of the phreatic line, such as the purple dash-line in Fig. 9. This trial phreatic line will be automatically corrected during the computational process to satisfy the hydraulic boundary condition until the steady-state seepage flow condition is achieved, thus giving rise to the final phreatic line. In SPH, once the trial phreatic line is determined, any SPH particle located below this line will be assigned an initial water pressure head, whose magnitude is inversely proportional to its vertical distance to the phreatic line. Our numerical tests with SPH confirm that the final prediction of the phreatic line is not sensitive to its initial guess.

Similar to the phreatic line, an initial guess is also required to identify the location of free-seepage surfaces. Subsequently, a boundary condition, namely the “ponding” pressure head condition, is imposed on the entire free-seepage surface boundary to satisfy the following equation:

$$h_w|_\Gamma \leq h_w^{\max} = 0 \quad (71)$$

Eq. (71) ensures the water pressure head on the free-seepage surface boundary (or open boundary) not greater than zero, and it holds for the entire geometric boundary that opens to the atmosphere. As a result, any open boundary

can always be treated as the free-seepage surface boundary, to which the “ponding” condition is implied. In SPH, the employment of the “ponding” to boundary particles means scanning these particles at the end of each time step. If its water pressure head was found to be greater than zero, it would be switch back to zero; otherwise, it would be updated as other real particles using Eq. (62). A detailed example of the implementation and the corresponding results will be presented and discussed in Section 5.

In addition, our newly proposed SPH formulation, although helped to improve the overall accuracy of SPH approximation for the second derivatives by removing associated errors source terms, produces undesirable and adverse effects at the free-surface boundary. In particular, taking away the error source term from the second derivative on free-surface boundary particles, (i.e. the second term on the right hand-side of Eq. (57)), virtually imposed an undesirable water flux on these boundary particles, which caused inaccurate seepage flow predictions in some cases. To avoid this issue, one could place several layers of virtual particles outside the free surface to avoid the kernel truncation, which is not an idea treatment because it requires extra computational costs to place these virtual particles. Here, a simpler approach is proposed by simply applying the following equation to SPH particle located on free-surface boundaries:

$$\frac{dh^i}{dt} = \frac{1}{\tilde{C}_{Sr}} \left\{ \sum_{j=1}^N V_j \bar{k}_{ij}^{mn} [(h^j + z^j) - (h^i + z^i)] D^{mn} \tilde{F}_{ij} \right\} \quad (72)$$

This treatment removes an undesirable water flux on particles located in the free-surface boundaries, where the boundary truncation occurs, and thus ensure accurate seepage predictions. It is noted this treatment does not involve extra computational cost as one would always need to identify these boundary particles on free-surface boundaries impose the ponding condition. Verification results will be given in Section 5.

#### d. Impermeable interfaces and impervious boundaries

In this paper, an impermeable interface refers to a thin layer of internal water-resistant structures, such as sheet pile walls and geomembrane walls, while an impervious boundary is used to indicate general water-resistant structures inside the porous medium with considerable thickness, such as clay cores with very low permeability. Both the impermeable interface or impervious boundary can be expressed by the following hydraulic condition:

$$|q_x|_\Gamma = |q_y|_\Gamma \approx 0 \quad (73)$$

Eq. (73) indicates that no water flux can occur over impermeable boundaries. While the implementation of impervious boundary is straightforward in SPH, the implementation of an impermeable interface is not that straightforward due to the summation nature of SPH that can extend its integral domain to the other side of the impermeable interface.

In SPH, boundary particles can be used to represent impervious boundaries (see Fig. 9) and impose the impermeable condition across the boundaries. These boundary particles are generated within the impervious boundaries and share the same material properties as adjacent soil particles. Furthermore, their hydraulic properties are constantly updated during the computation process to ensure that condition (73) is satisfied locally (i.e. inside the supporting domain of each SPH particle). To enable this for imposing impermeable boundary conditions, the hydraulic properties of boundary particles are updated as follows:

$$H^v = H^k; h^v = h^k; \text{ and } \mathbf{k}^v = \mathbf{k}^k \quad (74)$$

where the subscript “v” denotes boundary particles within the support domain of the real solid particle  $k$ . Eq. (74) indicates that all boundary particles located within the support domain of a real soil particle share the same hydraulic properties of this soil particle. Accordingly, condition (73) is satisfied automatically locally within the support domain, and thus ensuring no hydraulic head gradient takes place on the impermeable boundary. Similarly, an impermeable interface (see Fig. 9) can be modelled by preventing water flux from flowing across this boundary. For this reason, there is no need to explicitly modelled impermeable interfaces, as very often, these types of boundaries are very thin structure comparing to the overall length of the problem domain, and thus often requiring very fine resolution to represent the structures. A simple way to impose this boundary condition is to cut off the particle interaction pairs that cross these interfaces.

**Table 3**

Soil parameters for 1D infiltration test.

Permeability of saturated soil	$k^{sat}$	1.0 m/day
Saturation of saturated soil	$S_{sat}$	1.0
Residual saturation	$S_{res}$	0.23
Porosity	$n$	0.4
SWCC parameter	$\alpha_l$	$2 \text{ m}^{-1}$
The bulk modulus of water	$K_w^{sat}$	$2 \times 10^6 \text{ kPa}$
The bulk modulus of soil	$K_s$	$2 \times 10^5 \text{ kPa}$

### e. Spring boundary

This type of boundary condition is often encountered when the groundwater table is higher than the ground surface of a small domain located inside the problem domain, as highlighted in Fig. 9. In this case, seepage water emerges to the ground surface and forming a spring. To handle this boundary in SPH, the boundary, where the spring is anticipated to occur, is firstly located and treated as a free-seepage boundary, and thus Eq. (71) is applied. Subsequently, if the computational elevation of the phreatic line is lower than this boundary, no further step is required since the spring does not exist. Otherwise, spring occurs, and then the Dirichlet Boundary condition or “ponding” condition can then be applied to the spring’s location to defined the potentially highest total head. An example of this type of boundary will be presented in Section 5.

## 5. Numerical simulations

In this section, several well-known transient seepage problems are conducted using the proposed SPH framework, and the obtained results are compared against theoretical or FEM solutions to verify the proposed SPH model. SPH simulations are conducted on both regular particle system and non-regular particle system using the Voronoi distribution to demonstrate the robustness of the proposed numerical framework.

### 5.1. Example 1: 1-D infiltration/evaporation

This first example is designed to demonstrate the accuracy of the proposed formulation, comparing to with the traditional second derivatives formulations [59,61], in predicting 1D transient seepage flows with known analytical solutions. In this example, one-dimensional water infiltration and evaporation tests in an unsaturated soil column are considered, and only regular particle distribution is used here to enable tracking the change of pressure in the soil column from particles in the same vertical layer. Fig. 11a shows the initial condition for a one-dimensional infiltration problem. A soil column of 3 m height is modelled by a set of uniform distribution of SPH particles, and each is located at a spacing distance of 0.02 m from the other. The groundwater table is set at the bottom of the soil column, and a negative PWP head of  $h = -z$  is assigned to all SPH particles as their initial unsaturated condition.

In the infiltration test, the upper surface of the soil column is exposed to an infiltration rate of  $Q = 0.1 \text{ m/day}$ . A simplified SWCC and permeability functions are applied in this case [85]:

$$\begin{aligned} S_r &= S_{res} + (S_{sat} - S_{res}) \cdot e^{-\alpha_l|h|} \\ k &= k^{sat} \cdot e^{-\alpha_l|h|} \end{aligned} \quad (75)$$

where  $\alpha_l$  is a material parameter; and  $k^{sat}$  is the saturated permeability of water. Table 3 shows all soil properties and the constitutive parameters required for the simulation.

The entire transient unsaturated seepage process is simulated for 5 days with a fixed time step size  $\Delta t = 2.4 \times 10^{-5}$  days until the steady-state seepage flow condition is reached. Fig. 11 shows the evolution of the hydraulic head in the soil column, while Fig. 12a shows the calculated PWP head profiles at different time intervals. It can be seen that the proposed SPH model captures well the analytical solutions by Gardner [85]. In contrast, the SPH model employing traditional second derivative formulations [59,61] could not provide the exact solution to this 1D infiltration problem, as shown in Fig. 12b.

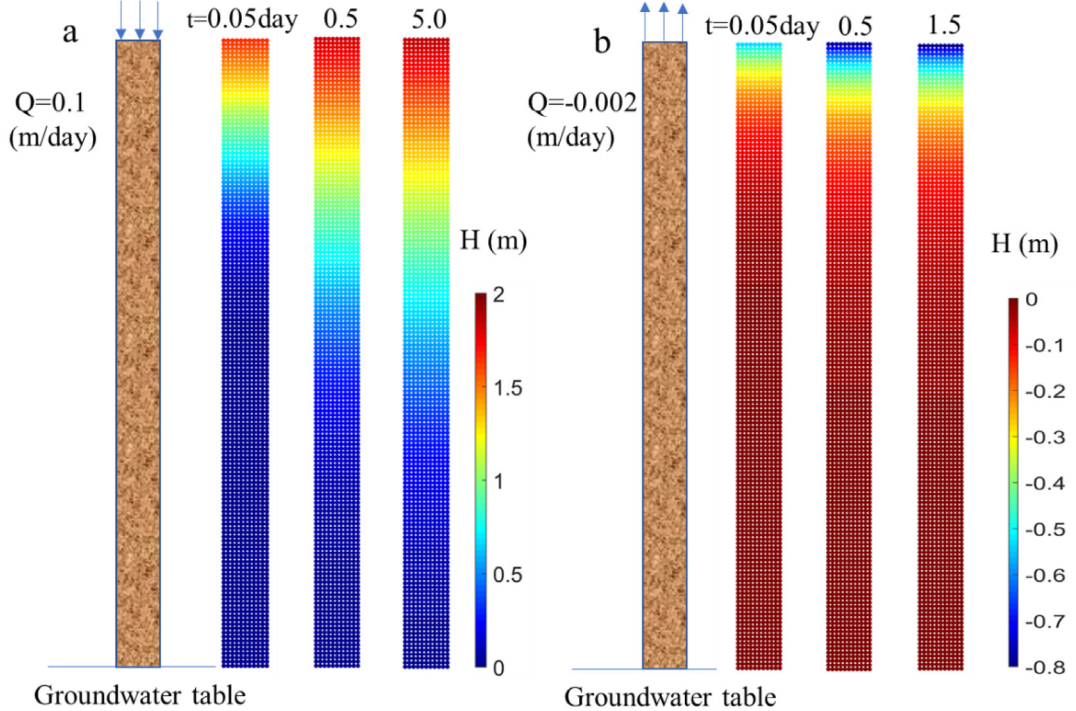


**Fig. 11.** Evolution of hydraulic head in SPH simulations of unsaturated seepage flow: (a) 1D water infiltration in a soil column and (b) 1D water evaporation in a soil column.

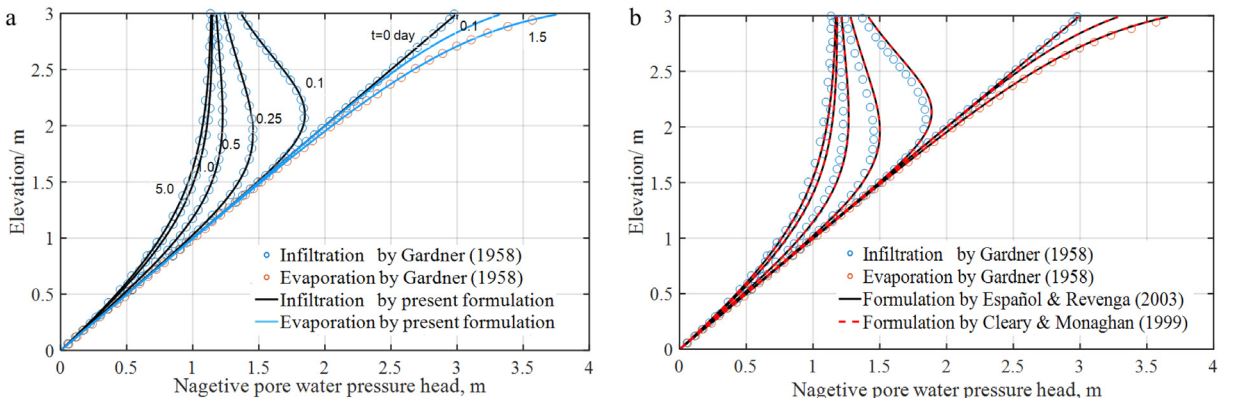


**Fig. 12.** Comparisons of the proposed SPH formulation and existing ones in predicting 1D water infiltration and evaporation problems at several time intervals.

The soil column problem is re-analysed for the case of evaporation by applying a negative flux rate  $Q = -0.002 \text{ m/day}$  on the upper surface (i.e. the first layer of particles), and the evolution of the hydraulic head in the soil column is shown in Fig. 11b. Again, it can be seen that the drying process reaches a steady state at around 1.5 days, and the negative pore-water pressure head profiles agree well with the theoretical solutions by Gardner [85] (see Fig. 12a). The traditional SPH formulations again failed to exactly reproduce the analytical solution (see Fig. 12b). These results indicate that the proposed SPH formulations work well in one-dimensional cases.

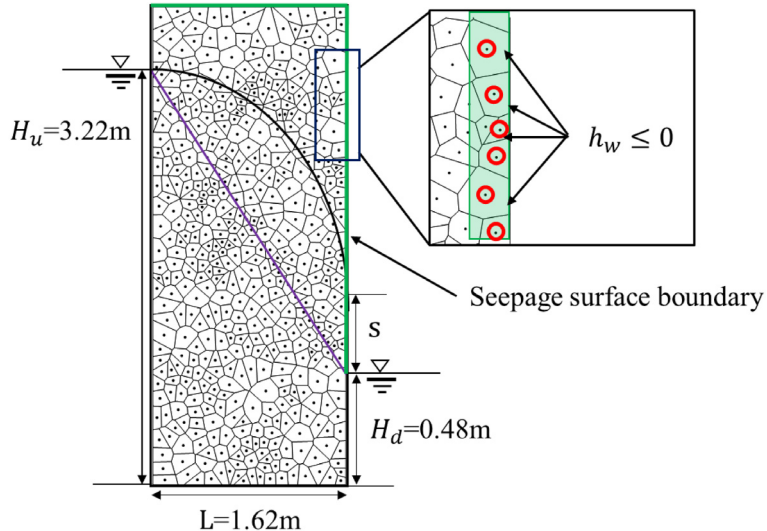


**Fig. 13.** Schematic diagram and boundary conditions of a homogeneous rectangular earth dam (i.e. Muskat problem). (For interpretation of the references to colour in this figure legend, the reader is referred to the web version of this article.)

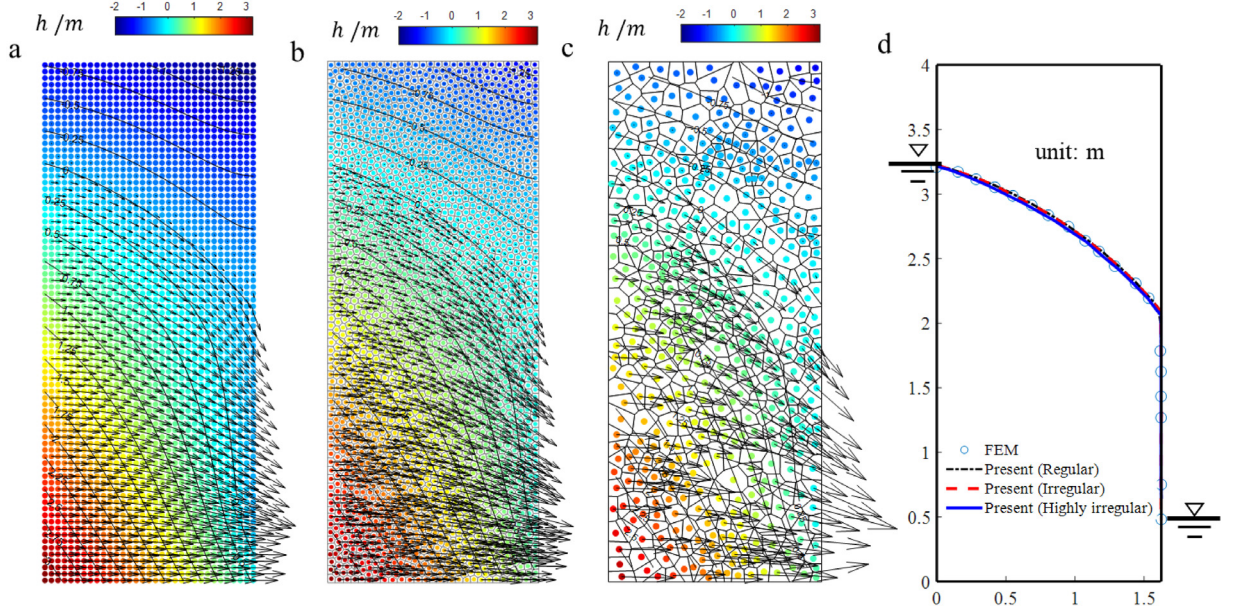
### 5.2. Example 2: Muskat unsaturated seepage flow problems

This example demonstrates the capability of the proposed SPH framework in predicting free-seepage surface through homogeneous and isotropic porous media using both uniform and random particle systems. In this example, a vertical cross-section of an unconfined groundwater flow system in a homogeneous earth dam underlain on an impervious base is considered and shown in Fig. 13. Such a problem is commonly known as the *Muskat problem* [2,3,86], where the phreatic line and seepage surface are unknown prior to the analysis.

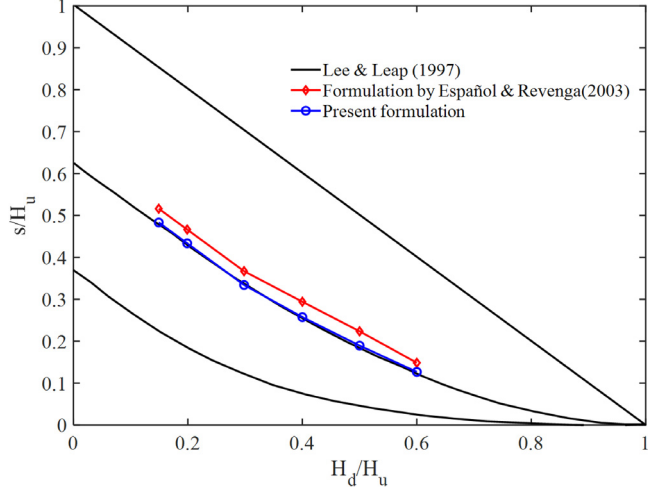
Fig. 13 shows the initial geometry and boundary conditions for the *Muskat problem* considered in this example. The overall length of the earth dam is 1.62 m. The groundwater table is 3.22 m upstream, and a lower water level of 0.48 m is assigned to the downstream boundary, above which the free-seepage surface boundary condition is considered and marked as green solid-line in Fig. 13. The “ponding” condition is directly applied to SPH particles which lie on the free-seepage surface boundary, as illustrated by the zoom-in section in Fig. 13. Furthermore, an initial phreatic line is assumed to be a linear line and marked as a purple line in Fig. 13. Three particle configurations with different levels of randomness are considered to evaluate the performance of the proposed SPH framework in predicting the seepage flow. They include a uniform particle system with 2672 SPH particles, an optimised Voronoi particle system with 2725 SPH particles and a highly irregular and coarse particle system with only 501 SPH particles.

Fig. 14 shows the results predicted by the proposed SPH framework and their comparison to FEM (Plaxis-2D) solutions. The calculated active pore-water pressure head on both particle systems using the present formulation agrees well with each other, as shown in Fig. 14a for the uniform particle system, Fig. 14b for the optimised Voronoi particle system and Fig. 14c for the highly irregular and coarse particle system. The specific discharge vector is illustrated with black arrows, indicating the change in seepage velocity from the upstream to the downstream. The most considerable seepage velocity occurs near the water table downstream and is well captured by the proposed SPH model on both particle systems. It should be emphasised here that, even though particles are highly disordered in Fig. 14b and highly irregular and much fewer in Fig. 14c, the predicted contour lines of the pressure head is the same and as smooth as those predicted on the uniform particle system (see Fig. 14a), indicating the superior feature of the newly proposed SPH formulation for the second derivatives, which yields highly accurate results on a disordered particle system. Besides, the predicted phreatic line and seepage surface in both particle systems are in excellent agreement with the reference results predicted by the commercial Plaxis-FE 2D, as shown in Fig. 14d.

To further demonstrate the performance of the newly proposed SPH model, the highly irregular particle system in Fig. 13 is adopted herein again to predict the seepage length under different downstream conditions (i.e.,  $H_d$ ).



**Fig. 14.** Predictions of active pore-water pressure head, seepage surface and flow field in a homogeneous rectangular dam using the newly developed SPH model: (a) regular particle system; (b) random Voronoi particle system with optimisation; (c) highly-random Voronoi particle system without optimisation; (d) Comparisons among SPH and FEM (Plaxis 2D) results.



**Fig. 15.** SPH prediction of the seepage length in Muskat problem using the present and the existing second derivatives formulation.

For the comparison purpose, only formulation proposed by Español & Revenga [61] is considered, though similar results could be achieved using the standard SH formulation proposed in [59]. Fig. 15 shows a comparison of the predicted seepage lengths between different approaches and theoretical solutions. It can be seen that, even with a very small number of particles and a highly random particle configuration, the newly proposed SPH formulation still produces accurate results, which agree well to the theoretical solutions derived in Lee & Leap [7]. In contrast, the traditional SPH formulation by Español & Revenga [61] overestimated the seepage length, suggesting that this traditional SPH formulation is less accurate on an irregular particle. Nevertheless, the results predicted by the standard SPH formulations should approach the theoretical solutions as the number of particles used to represent the computational domain increases and their distribution is more regular. Overall, the above results suggest that the newly proposed SPH framework is more accurate than the existing ones and could capture well the unsaturated

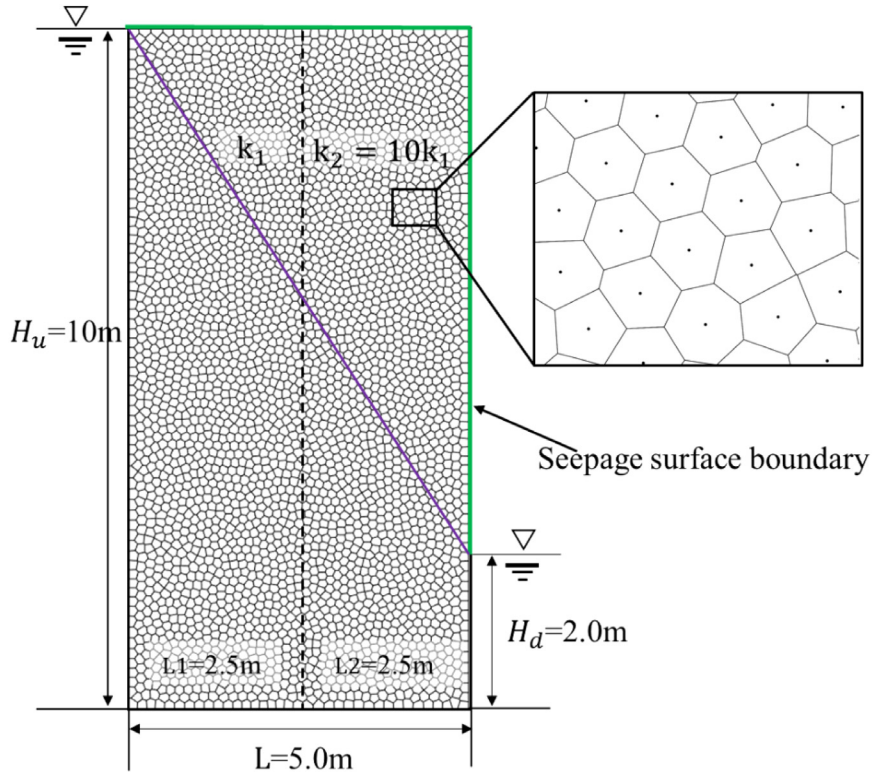


**Fig. 16.** Schematic diagram and boundary conditions of a non-homogeneous rectangular earth dam. The trial linear phreatic line is marked in purple and the non-uniform particle system using Voronoi mesh is used to represent the computational domain.

seepage flow problems on homogeneous porous media. The numerical results produced by the new SPH model are comparable with FEM and analytical solutions, even when the simulations are conducted on a highly irregular particle configuration or using a very small number of SPH particles, thanks to the proposed highly accurate SPH formulation for second derivatives.

### 5.3. Example 3: Non-homogeneous rectangular earth dam

To further demonstrate the capability of the proposed SPH framework for modelling free-seepage surface problems involving different material properties, a non-homogeneous rectangular earth dam is considered in this example. Fig. 16 shows the geometry setting and boundary conditions of the non-homogeneous earth dam. It consists of two vertical soil columns placing adjacent to each other and having different permeabilities. The soil column on the left-hand side has a permeability  $k_1 = 1.0 \text{ m/day}$ , while that on the right-hand side has a permeability  $k_2 = 10.0 \text{ m/day}$ . It can be seen that this problem involves discontinuity in the hydraulic coefficient in the middle section of the dam. Within the FEM context, Bear [74] suggested dividing the entire domain into subdomains along the surface of discontinuity and solve each subdomain simultaneously, so that the problem can be reduced to the standard homogeneous Muskat problem discussed above. In this case, the predicted seepage surface downstream of the first soil column will become the upstream boundary condition for the second soil column. A continuity condition for water flux and pressure then needs to be satisfied on the disjoining interface. However, the pressure and water flux for both sides are unknown a priori, leading to extra difficulties in numerical implementations. In this study, SPH stands out with no requirement of the spatial division of the domain and straightforwardly solve the entire problem using a single set of boundary conditions given in Fig. 16.

The above non-homogeneous problem was solved under both uniform and non-uniform (i.e. Voronoi) particle systems. For the uniform particle system, 3321 particles with an initial spacing of 0.125 m are used to generate

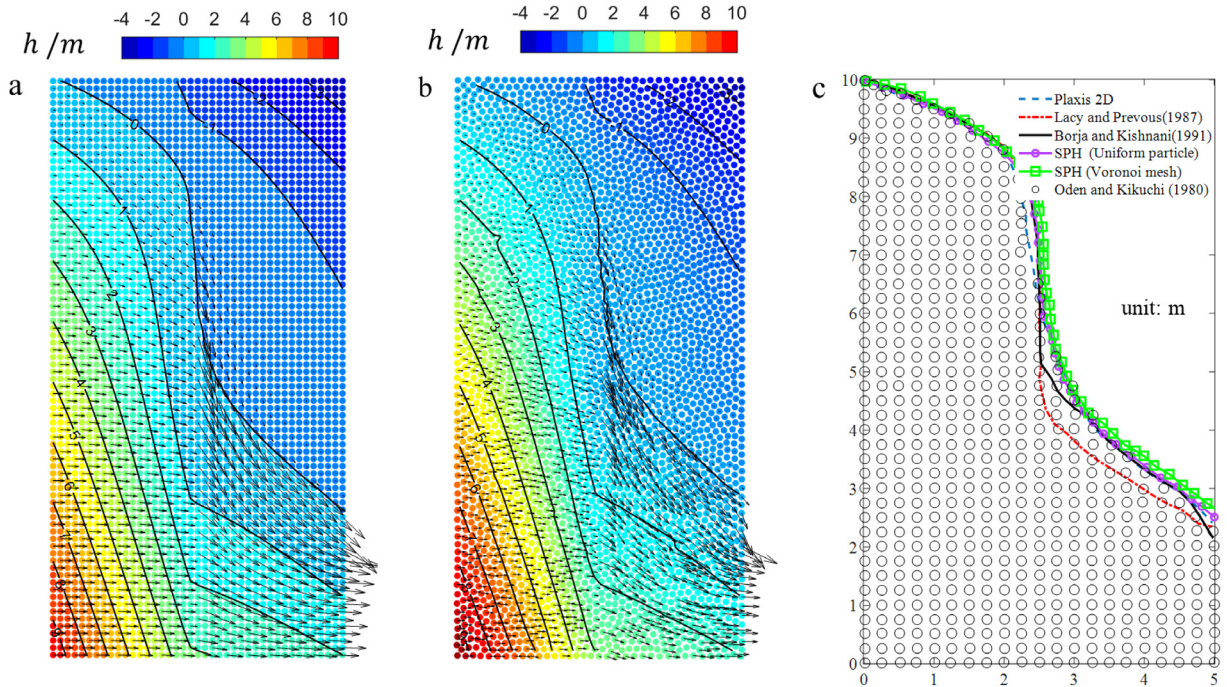


**Fig. 17.** The contour of the active PWP head, the seepage surface, and the water flow field of a non-homogeneous rectangular dam. (a) Results by Standard SPH method; (b) Results by the proposed random particle system in SPH. (For interpretation of the references to colour in this figure legend, the reader is referred to the web version of this article.)

the computational domain, whereas the same number of irregularly distributed particles are adopted for the random Voronoi particle system, as shown in Fig. 16. The boundary conditions are imposed on the upstream and downstream boundaries, which are similar to those adopted in the previous example of the Muskat problem.

Fig. 17 shows the predicted seepage flow through the non-homogeneous earth dam by SPH and its comparison to several numerical results available in the literature. It can be seen that the distribution of active pore-water pressure head and water flow patterns in the non-homogeneous earth dam is well captured by the proposed SPH model on both particle systems. The contour lines of the water pressure head exhibit a rapid change on the interface due to the sudden change in permeability. At the same time, an increase in the seepage velocity, indicated by the increasing size of black arrows, is also observed once the water flow enters the porous medium with higher permeability (i.e. the right soil column). Thanks to the symmetric form of the SPH discretisation for the flow governing equation, a smooth transition of water pressure and water flux was well preserved in the adjoining region. It is also worth noting here that the arithmetic mean value of the water permeability is adopted in this paper, which is proven to be able to handle the seepage problems with discontinuity in the adjoining interface very well. Finally, a comparison between SPH and literature results for the prediction of phreatic lines is shown in Fig. 17c. The phreatic lines predicted by SPH on the uniform and Voronoi particle systems are marked in purple with circle markers and in green with square markers, respectively, along with other solutions available in the literature [4–6]. Again, the results predicted by the newly proposed SPH framework agree well with others in the literature, especially to that of FEM (Plaxis-2D). The minor deviation among SPHs and FEM results can be attributed to the difference in how the phreatic line is extracted from each method. Overall, the very good agreement between the predicted results and those available in the literature indicate that the newly proposed SPH model is capable of handling the unsaturated seepage flow problems with discontinuity in the material property.

#### 5.4. Example 4: Trapezoidal porous domain

Unsaturated seepage flows through a trapezoidal embankment is one of the popular case studies, besides the rectangular earth dam. Comparing with the flows through a rectangular dam, the seepage surface in the trapezoidal

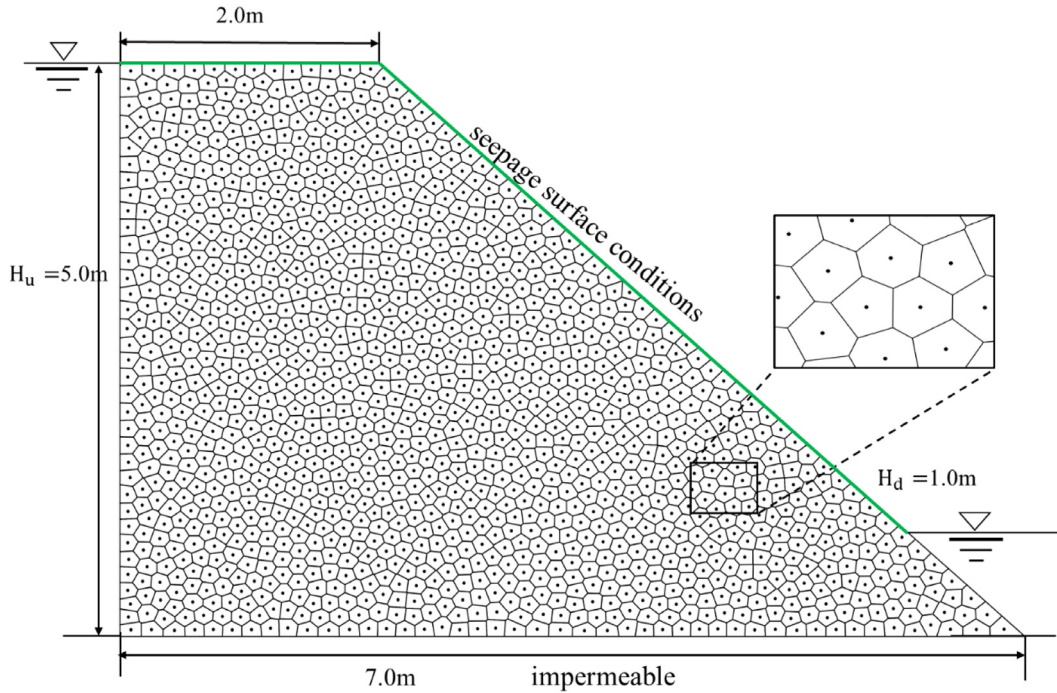


**Fig. 18.** The geometry and boundary conditions of a trapezoidal embankment and its corresponding random particle system associated with Voronoi mesh.

embankment is expected to occur along an inclined dam surface. In this example, the proposed SPH framework is applied to solve unsaturated seepage flows through a trapezoidal embankment, and numerical results are compared with well-documented data available in the literature [1,5,6,8]. This example is also considered as an example to demonstrate the efficiency of the proposed boundary implementation technique in capturing the seepage surface in an inclined interface besides the vertical ones in Examples 2 and 3. Fig. 18 shows the geometry of the trapezoidal embankment and boundary conditions required to solve the problem. All material properties required to solve this problem have been listed in Table 1 and Section 2.5. The problem is solved on both regular and random particle systems using the weighted Voronoi tessellation discretisation, where the latter one is shown in Fig. 18. In both cases, 1524 SPH particles are used to represent the porous medium. Boundary conditions are imposed directly on soil particles located on the boundaries, without creating boundary particles, though the same results could be achieved when boundary particles are adopted.

Fig. 19 shows the distribution of the predicted active pore-water pressure and water flow patterns in the trapezoidal embankment. The final shape of the groundwater table is found to be a curved line with the upstream end normal to the upstream equipotential line (i.e. the upstream slope) and the downstream end tangent to the downstream slope, over which the water seeps out from the embankment. It is also observed that the most significant seepage velocity, as marked by the black arrow, occurs near the downstream water table. The calculated phreatic line and seepage surface under both particle systems are highlighted in Fig. 20. It can be found that the results predicted by the newly developed SPH framework agree well with the result reported in [1], i.e., the predicted seepage surface is tangent to the slanted face, which is more accurate than results reported in [5,6,8] in the early time, where the calculated seepage surface is off the slope surface. This difference can be due to the fact that those early results in [5,6,8] were obtained using the fixed mesh with the “Extended Pressure” method, of which the accuracy was highly dependent on the mesh constructions for complex geometries [2,3], causing the minor error in this case. More importantly, the SPH results on the random Voronoi particle system is consistent with those obtained on the regular particle systems, thanks to the newly proposed SPH formulation for the second derivatives that help to improve the accuracy of random particle configurations. These results suggest that the proposed SPH framework can handle well seepage problems involving complex geometries.

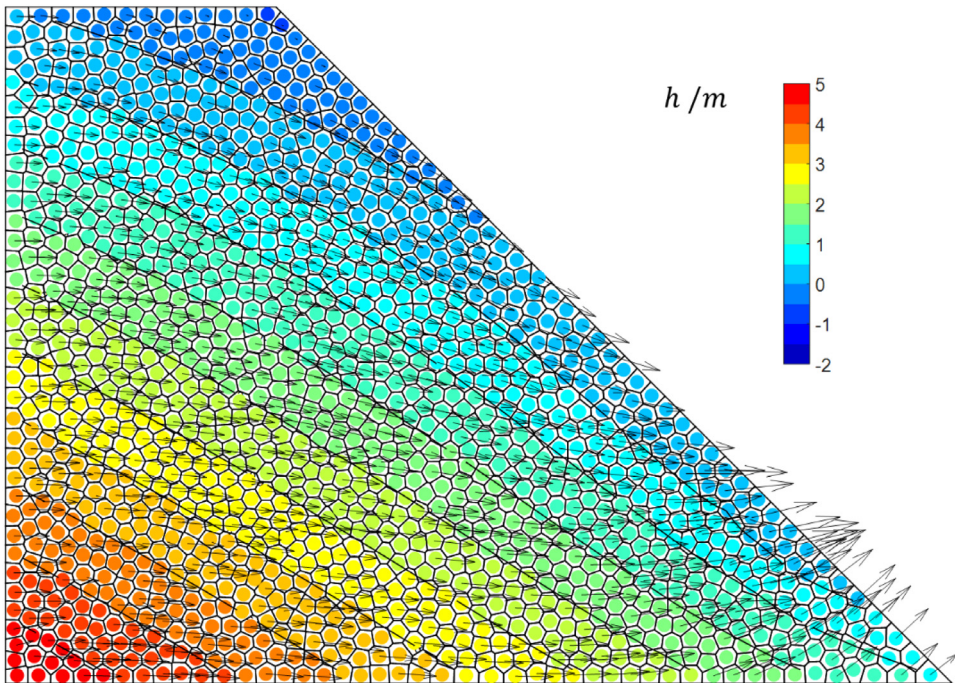


**Fig. 19.** Simulations of active PWP head, seepage surface and water flow field in a trapezoidal cross-section dam by the proposed system based on Voronoi mesh in SPH.

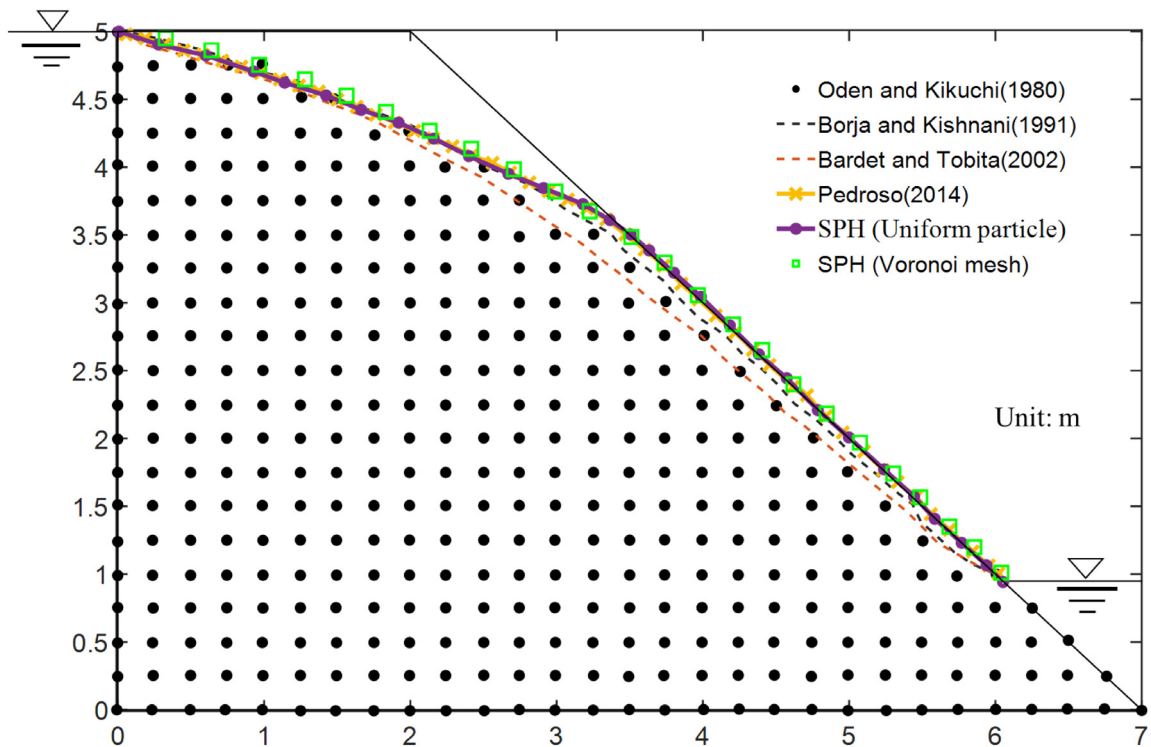


**Fig. 20.** Calculated phreatic line and seepage surface for a homogeneous trapezoidal dam in comparison with other solutions [1,5,6,8].

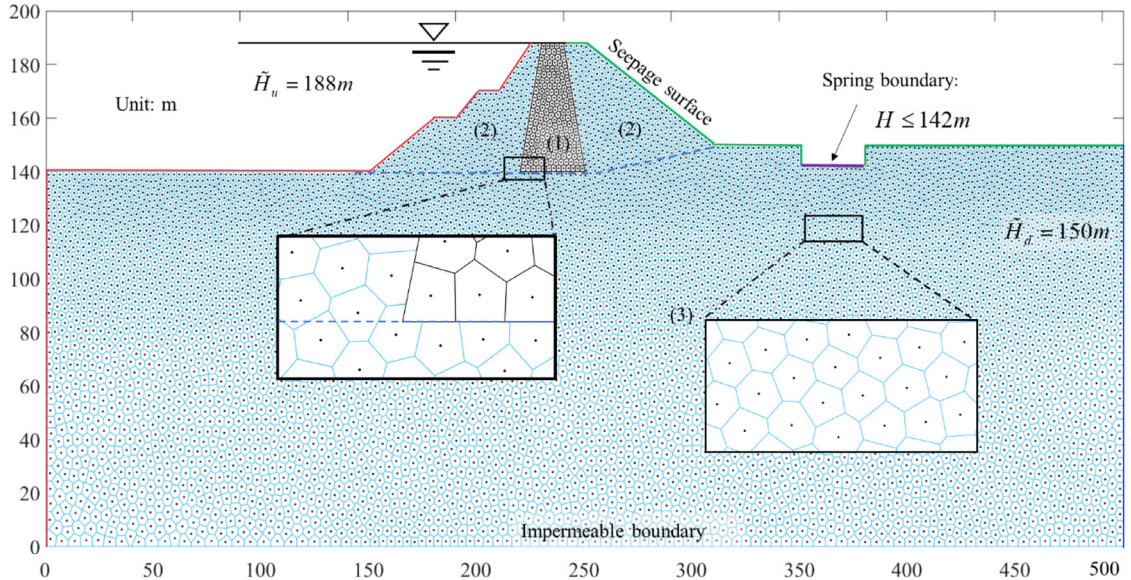


**Fig. 21.** Geometry and boundary conditions of a large earth dam with a very low permeability clay core and its corresponding spatial discretisation using multi-size Voronoi particles. (For interpretation of the references to colour in this figure legend, the reader is referred to the web version of this article.)

### 5.5. Example 5: Unsaturated seepage flow in a large embankment dam

To demonstrate the efficiency of the proposed model in handling large-scale seepage problems using a multi-resolution particle system, in this example, a large embankment dam with a clay core, which was previously studied by [1,2], is considered. This example also serves as an excellent mean to assess the efficiency and performance of the proposed SPH model in automatically locating free-seepage surfaces on problems involving complex boundaries and significant hydraulic property differences inside the embankment. The clay core has a very low permeability to limit the hydraulic gradient across the embankment, and thus reducing the risk of embankment failure. Fig. 21 shows the dimension of the embankment and its hydraulic boundary conditions. The embankment consists of three major regions with significant differences in saturated conductivities. Region (1) refers to the clay core with a very small hydraulic conductivity of  $k_{sat}^1 = 10^{-9}$  m/s, while the other two regions, (2) and (3) have significantly large hydraulic conductivities of  $k_{sat}^2 = 1$  m/s and  $k_{sat}^3 = 0.1$  m/s, respectively. The hydraulic boundary conditions are designed as follows. A constant total head of 188 m was assigned to all particles located on the soil surface on the left reservoir (as marked in red in Fig. 21), while on the downstream boundary, a constant total head of 150 m was pre-described (i.e. marked in blue in Fig. 21). The seepage surface boundary (i.e., “ponding” condition  $h|_T \leq h^{max} = 0$ ) was imposed to particles on the right surface of the reservoir, where the seepage surface is expected to occur (as marked by the green lines in Fig. 21). Furthermore, the “ponding” condition for the spring boundary was set as  $H \leq 142$  m for those particles located on the ground surface of the spring (i.e. marked in purple in Fig. 21). The unsaturated condition for the soil elsewhere in the entire embankment is specified by an initial water pressure head as  $h = -z$ , while other required hydraulic constitutive parameters are given in Table 1.

One of the key challenges in solving this problem is that the computational domain involves strong inhomogeneity, and the seepage surface is expected to occur on more complex mixed boundaries, consisting of slanted, horizontal and vertical surfaces, in addition to the spring boundary condition considered, making it challenging in determining the length of the seepage surface, particularly for FEM where variational inequality formulations or even mesh adaption technique are required [2,3]. Furthermore, within the context of SPH, the most challenging issue associated with solving this case is that the size of the embankment dam with the clay core is much smaller than the overall length and height of the entire computational domain, making the overall computational cost highly expensive if the regular grid with a sufficiently small size is adopted to capture the details of the embankment and the clay core. To address this challenge and provide a numerical solution to large-scale seepage problems, the newly

proposed SPH framework with multi-resolution discretisation is adopted. This attempt is worth to be adopted since it provides a balance between the accuracy and computational costs for full-scale simulations. It has not been used with SPH in the past to predict unsaturated seepage flows through geotechnical structures.

To establish a variable discretisation particle system suitable for SPH simulations, at first, the entire computational domain is divided into three sub-domains according to the elevation for different resolution requirement. Thereafter, 2411 and 3165 SPH particles are randomly generated in the sub-domain of  $0 < z < 80$  m and  $80 \leq z < 120$  m, respectively, whereas 2246 particles are placed in the rest of the embankment. After that, the WVT technique is adopted to re-arrange the particle to obtain the Voronoi particle system shown in Fig. 21; therefore, a total of 8022 particles are used in this case. Similar to the previous examples, appropriate boundary conditions are imposed on SPH particles located right on the hydraulic boundaries, and thus no boundary particles are used in this example.

Fig. 22 presents the numerical results predicted by the proposed SPH framework at several time intervals. It is found that the water flow pattern and seepage velocity in the earth dam is well captured by the proposed SPH model, as indicated by the contour plots of pressure head and black arrows, respectively. The seepage velocity exhibits a decreasing trend once the water flow enters domain (3) with a lower permeability under the dam, and it increases back when the water flow exists in this domain and entering domain (2) after crossing the clay core. Thus, the water flow concentrations can always be observed when water travels around the corners of the very low permeability clay core. The evolution of the active pore-water pressure head in the domain is also well described, showing a clear change of the phreatic line, as indicated by the red line with square markers in the figures. The phreatic level ascends over time from the lower sections to the final location until the steady-state seepage flow is reached. This demonstrates a transition process from unsaturated to saturated flow conditions, over which a real-time seepage flow that travels from the upstream to the downstream crossing the clay core is well described. The final morphologies of the phreatic line predicted [1,2] are also included in Fig. 22c and marked with blue diamond and black circles, respectively. It can be found that the final phreatic line predicted by the proposed SPH model matches well the reference results, even though the SWRC models and conductivity models are not the same.

It is worth emphasising here that our numerical procedure to obtain the above transient unsaturated/saturated seepage flow is completely different from that presented in [1] using FEM, where the calculated phreatic line descended from the upper surface of the embankment to its final location. In the approach presented in [1], the whole embankment was initially assumed to be fully saturated, and the solution to the final steady-state phreatic line was achieved by linearly lowering the hydraulic head on the seepage boundary on the right reservoir until reaching the spring boundary, which was assumed to be known in advanced. As a result, the final position of the steady-state phreatic line predicted in [1] heavily depended on the final hydraulic head boundary condition imposed on the right reservoir, i.e. the spring boundary in this case. Furthermore, although the final location of the seepage surface was well predicted in [1], the procedure to achieve its solution did not realistically reflect the transient seepage flow development. Nevertheless, the fully dynamic unsaturated–saturated transition seepage flow and the real-time evolution of the water flow are naturally captured by the proposed SPH model with only one single set of the boundary conditions imposed at the beginning of the computation. In addition to the good agreement between the proposed SPH model and other well-established methods, the above results suggest that random particle configuration with multi-resolution is possible in the proposed SPH framework. The difference in mean particle size varies from 2.5 m to 5.0 m, which is large enough to produce poor solutions in the conventional SPH model that makes use of standard SPH formulations. Nevertheless, thanks to the newly developed SPH formulation for the second derivatives, the proposed SPH framework could capture well the smooth transitions of water pressure and water crossing boundaries with different particle resolutions and random distribution.

Finally, to further illustrate the ability of the proposed approach to model the unsaturated/saturated transient seepage flows at large scales, much coarser Voronoi cells and thus requiring fewer particles are considered. The results for different resolutions are presented in Fig. 23. It can be seen that the final shape of the steady-state phreatic level can be well predicted, even with a very small number of particles, as much as 4403 and 2206 particles for such a large-scale problem. Very good agreements with the reference ones [1,2] are again achieved, suggesting that the proposed second derivative associated with the Voronoi diagram in SPH can provide reasonable accuracy in the random and multi-resolution particle system.

### 5.6. Example 6: Transient seepage in an anisotropic slope

Up to this point, the newly developed SPH framework has been well demonstrated for its capacity to accurately predict the unsaturated/saturated transient seepage flow problems. However, the readers should have noticed that all

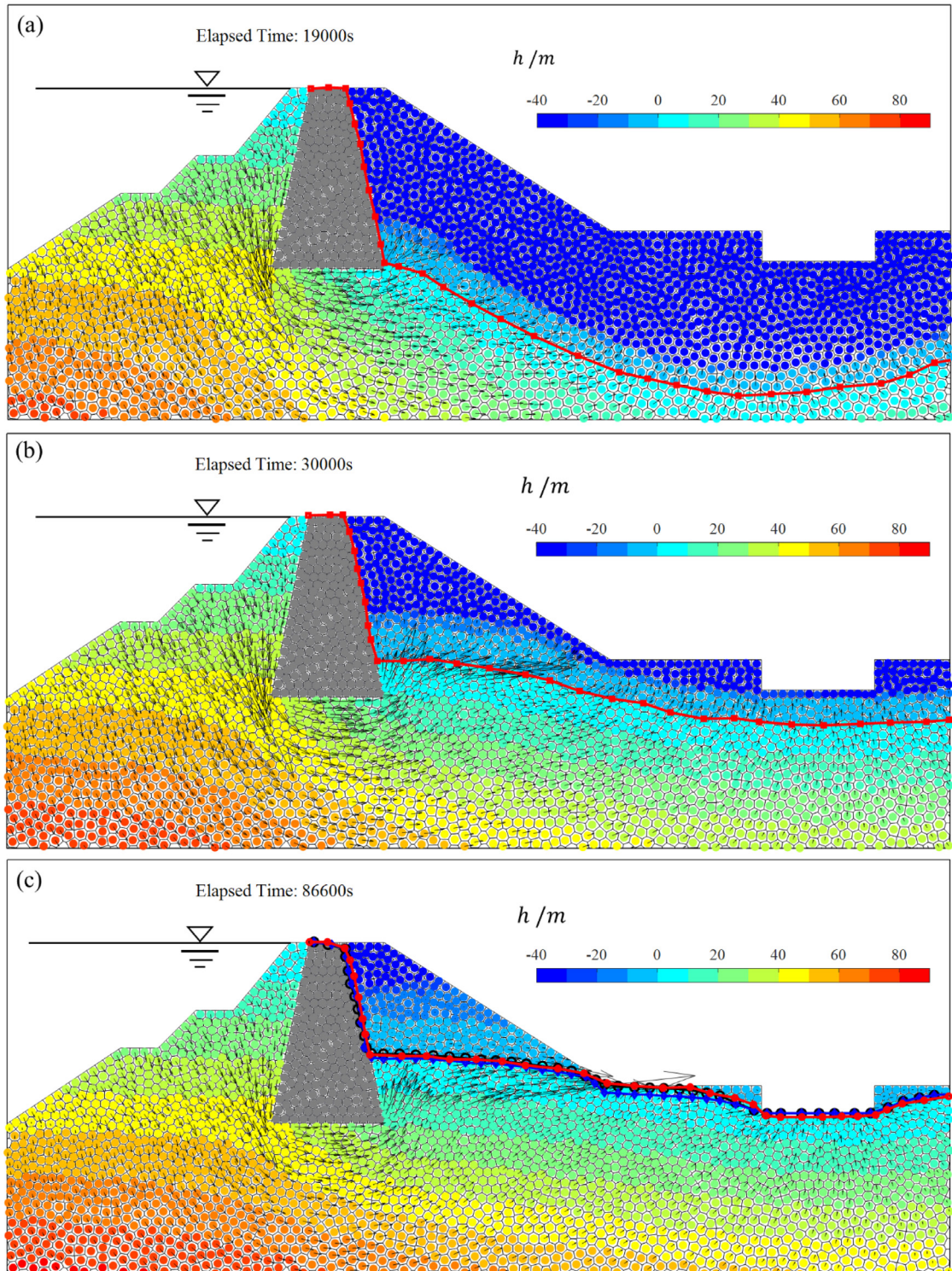


**Fig. 22.** SPH predictions of unsaturated seepage flow through an earth dam with a clay core and its comparison with the steady-state phreatic lines predicted by [1] and [2]. (For interpretation of the references to colour in this figure legend, the reader is referred to the web version of this article.)

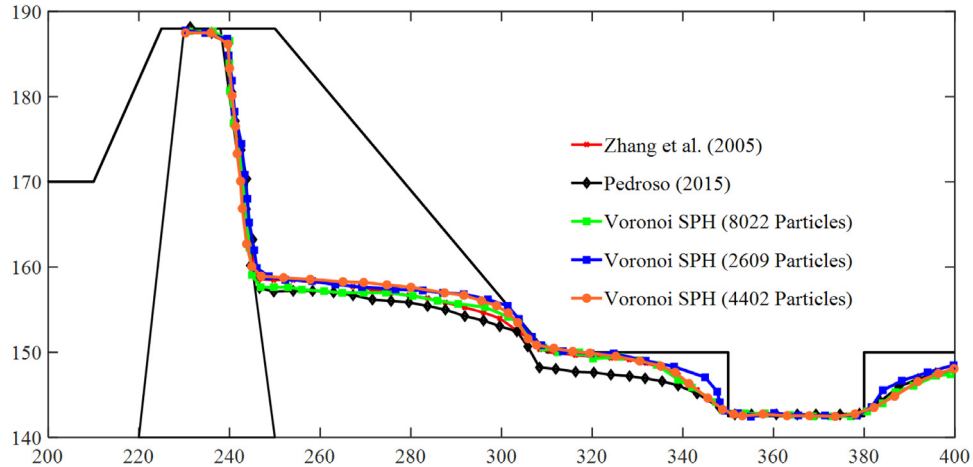


**Fig. 23.** SPH predictions of the final steady-state phreatic line using different particle sizes or Voronoi mesh sizes.

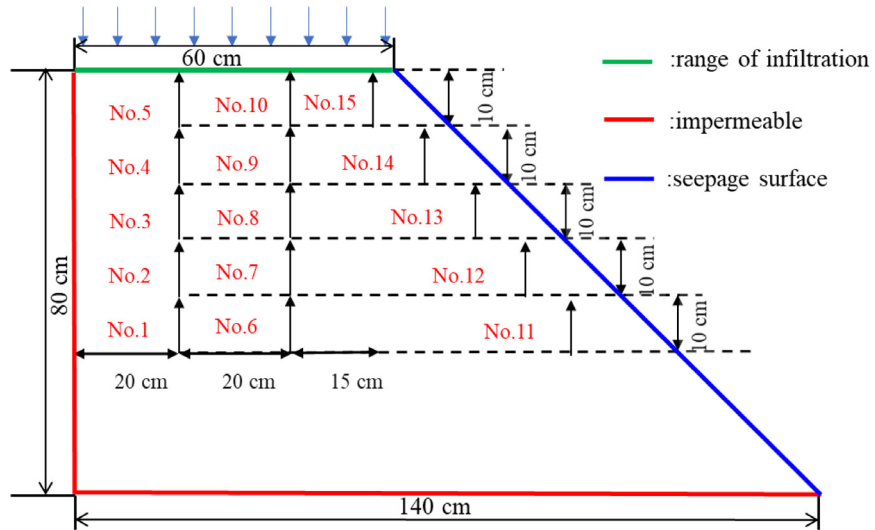


**Fig. 24.** The numerical setup for the rainfall infiltration test. (For interpretation of the references to colour in this figure legend, the reader is referred to the web version of this article.)

examples considered in the previous sections deal with isotropic soils, which share the same hydraulic conductivity in all directions. In reality, soils are anisotropic, and thus it is important for a newly developed numerical method to properly describe the transient seepage flows in anisotropic porous media. In this example, the capability of the newly developed SPH model to accurately capture transient seepage flows in an anisotropic porous medium is demonstrated by simulating rainfall infiltration through a slope embankment. Rainfall infiltration modelling is one of the important topics in seepage analysis because it provides critical information to evaluate changes in soil properties during rainfall and thus providing reliable information for assessments of stability and failure of earth structures. In addition to the complexity involving solving anisotropic seepage flows, another key challenge for SPH as well as other numerical methods in solving rainfall infiltration problems is to adequately describe the complete time-dependent unsaturated–saturated seepage transition process, in which the groundwater table rises due to rainwater accumulation at impermeable boundaries and reaching seepage surface boundaries.

Fig. 24 shows the geometry of the slope and hydraulic boundary conditions considered in this example. A water flux of  $Q = 0.003 \text{ m/min}$  is imposed to the upper slope surface (i.e. marked as green) to simulate rainfall infiltration condition. To facilitate the rainwater accumulation that causes an increase in the groundwater table, the left and

bottom boundaries (marked as red) of the slope were set to impermeable. On the other hand, the hydraulic boundary condition on the slope surface was set to seepage surface so that the accumulated rainwater can escape from this boundary. A total of 15 measuring points (i.e. marked as No.1 to No.15) are designed to monitor the evolution of pore-water pressure inside the slope during rainfall infiltration. Among these measuring points, No.11 to No.14 are located outside the range of direct water infiltration, which is important to evaluate the performance of the new SPH model in predicting anisotropy seepage flows. Both isotropic and anisotropic soils are considered in this example, with the latter one being achieved by setting the following hydraulic condition  $k_x = 0.4k_y$  and  $k_{xy} = k_{yx} = 0$ . To provide reference solutions for validation, the FEM (Plaxis-2D) are also conducted utilising the same model geometry and boundary setting conditions. In both methods, an initial negative pore-water pressure of  $-8$  kPa is assigned to the entire domain to generate an initially unsaturated slope condition. Other required hydraulic parameters are shown in [Table 1](#).

A total of 2050 particles is used in the SPH model to represent the computational domain. These particles are uniformly distributed in a square lattice with a spacing distance of 0.02 m, although the same results could be achieved on the Voronoi particle system, as demonstrated in the earlier sections. In addition, an adaptive time-step scheme is adopted to simulate the transient seepage flow from unsaturated to fully saturated states. In the unsaturated seepage state, the time-step size changes with respect to the minimum value of the specific moisture term, and once the seepage water reaches the bottom boundary and forms a fully saturated condition, the time-step decreases to  $\Delta t = 3 \times 10^{-5}$  min and remains unchanged for fully saturated seepage flows. It is noted that the smallest time-step size of  $\Delta t = 3 \times 10^{-5}$  min could be used to analyse the seepage flow in both unsaturated and saturated regimes. However, this approach is not recommended as it significantly increases the overall physical computational costs (i.e. computer running time) required to solve the transient unsaturated/saturated seepage flow problems. We tested our proposed adaptive time-step methodology and confirmed that the same results could be achieved by both approaches. However, by adopting the adaptive time-step scheme, the overall physical computational cost required to solve this is significantly reduced.

[Fig. 25a](#) and b show a comparison between the proposed SPH model and FEM (Plaxis-2D) for the evolution of the degree of saturation in the isotropic slope at several different time intervals. From the contour plot of the degree of saturation, a clear wetting process in the slope can be captured by the proposed SPH model, and the SPH results match well with those predicted by FEM (Plaxis-2D). For example, once the water flux is imposed on the upper surface of the soil slope, it starts gradually infiltrating into the soil under gravity. As the wetting processing, an increase in the saturation to nearly 70% can be seen, which forms a clear elliptic wetting front in the slope (i.e. T = 40 min). Due to the gravity, the seepage water travels mainly in the vertical direction and arrives at the bottom at around T = 65 min. Within this first 65 min, the largest degree of saturation is found to be around 70%, indicating that during this period, the slope is exhibiting an unsaturated seepage state, which is also a period where a large time-step size was used in the simulation. Subsequently, because of the undrained boundary, the infiltrated water is trapped at the left bottom corner and starts to accumulate (i.e. T = 74 min). This accumulated water content further increases to reach the degree of saturation  $S_{sat} = 100\%$ , leading a fully saturated zone at the left bottom corner. Once the fully saturated condition is observed in the computational domain, a smaller time-step size is required. It is also noted that before the water accumulation, the degree of saturation near the infiltration surface is higher than elsewhere; however, after water entrapment starts to develop at the bottom, the situation reverses. At the same time, with this transition from the unsaturated to fully saturated states, the fully saturated zone gradually develops inside the slope. Within the last 55 min, the trapped water at the bottom of the slope toward the right permeable slope surface and almost reaches this surface at around 120 min.

[Fig. 25c](#) shows a comparison between the proposed SPH model and FEM (Plaxis-2D) for the predicted negative pore-water pressure (PWP) at 15 monitoring points. Excellent agreements between the two numerical methods are achieved across all monitoring points, suggesting that the newly developed SPH model could capture well the transient seepage flow problems. However, there exist some noticeable differences between the results predicted by SPH and FEM, and this can be attributed to different ways adopted in each method to solve the seepage governing equations. In addition, a clear wetting process can also be seen from the evolution of the PWP presented in this figure. For example, as the infiltration front migrating downwards, the suction at No.5, No.10 and No.15 starts to decrease at around 5 min as these monitoring points are installed near the top slope surface, and gradually reaching their temporary equilibrium state at around 30 min, corresponding to a negative PWP of around  $-2.35$  kPa. With further progression of the wetting front downwards due to the gravity, the suction at other monitoring points follows

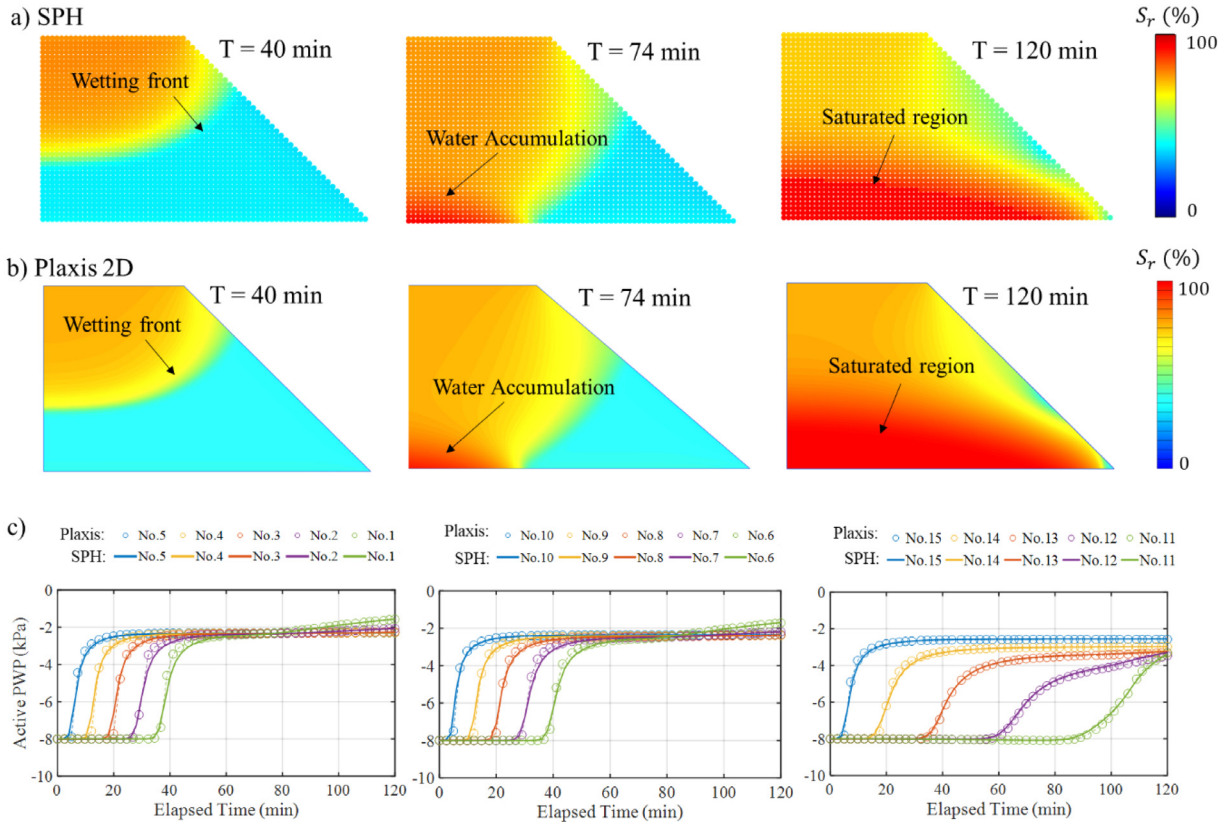


**Fig. 25.** The calculated evolution of the degree of saturation and active PWP in the soil tank for different time intervals with isotropic permeability. (a) Result by SPH; (b) Result by FEM (Plaxis-2D); (b) Comparison of the predicted active PWP in the measuring point.

the same trend, but reaching their temporary equilibrium state at different times, with further delay associated with those points located close to the bottom of the slope and toward the slope surface. The delay in the development of suction at monitoring points located close to the slope surface (i.e. No.11–No.14) can be attributed to the fact that the infiltration seepage flow first progresses in the vertical direction to reach the undrained boundary at the bottom, accumulating water before changing its direction to progress laterally to reach those monitoring points. During the temporary equilibrium state, the soil at all monitoring points is still under the unsaturated condition, which is evidenced by the negative PWP value at all points. As the infiltration seepage flow continues, seepage water gradually accumulates at the bottom slope, forcing the groundwater table to rise. As a result, the suction at the bottom monitoring points (i.e. No.1 and No.6) react to this change and further reduce after 85 min. The change in suction at monitoring point No.11 due to the increase in the groundwater occurs latest as this point is located close to the slope surface.

Next, the simulation is repeated for an anisotropic slope (i.e.  $k_x = 0.4k_y$ ) to further demonstrate the capability of the proposed SPH model in capturing complex seepage problems. Fig. 26 shows a comparison between SPH and FEM (Plaxis-2D) for the behaviour of the seepage flow inside the anisotropic slope. Again, excellent agreements between SPH and FEM (Plaxis-2D) are achieved, suggesting that the new SPH model could capture well the anisotropic seepage flow, thanks to the newly developed SPH formulation for second derivatives that can account for anisotropy diffusion. Comparing to the isotropic case, though there exists similarity in the saturation process as illustrated in Fig. 26, some differences can be noted. For example, due to the anisotropy nature ( $k_x < k_y$ ), less water content progresses in horizontal direction, which leads to the shape of this wetting front becomes more cursive close to the slope surface. Another difference is that the wetting front progresses much more rapidly in the vertical direction, which arrives at the bottom at around 60 min, whereas it is 5 min later for the isotropic case. Thereafter, the same water accumulation process can be observed, though the fully saturated region at the left

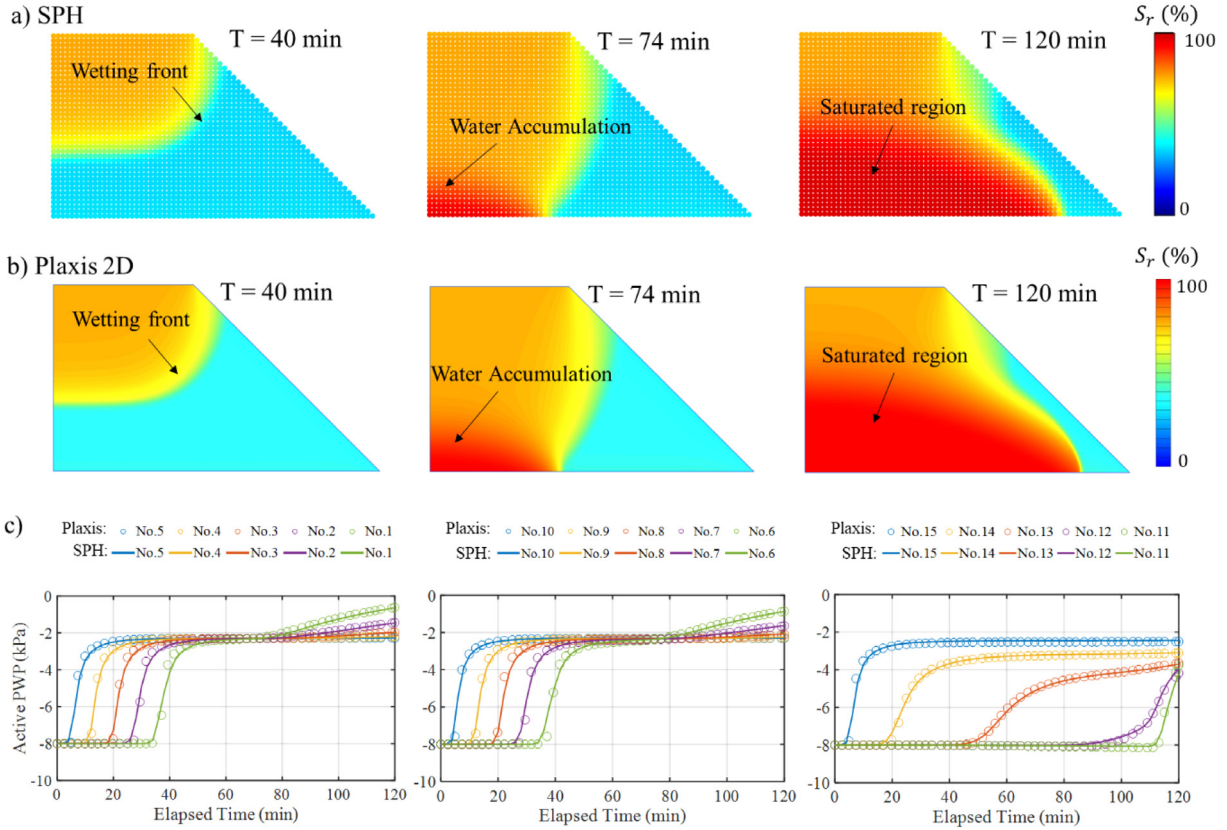


**Fig. 26.** The calculated evolution of the degree of saturation and active PWP in the soil tank for different time intervals with anisotropic permeability. (a) Result by SPH; (b) Result by FEM (Plaxis-2D); (b) Comparison of the predicted active PWP in the measuring point.

bottom corner develops faster than that of the isotropic case (see Fig. 25a and b). This is because a smaller horizontal permeability ( $k_x$ ) constraint the water travel toward the right boundary; thus, more water content is trapped, forming a more significant saturated zone in the soil tank. For the same reason, the entrapped water could not reach the open surface at 120 min (see Fig. 25). However, this arrival was captured in the isotropic case (see Fig. 25).

Fig. 26c shows the comparison of the predicted negative PWP between the presented method with FEM (Plaxis-2D) considering anisotropic permeability. Very good agreements with FEM (Plaxis-2D) for the active PWP measured at points No. 1 to No. 15 are achieved by the proposed SPH model. Comparing with the isotropic case, the main difference lies in the predicted pore-water pressure in the last 55 min, where the predicted curves go much more upwards, indicating that a much significant decrease in suction at these measuring points (i.e., No. 1 and No. 6). This phenomenon is contributed to the smaller permeability along the horizontal direction, by which accumulated water content could not be drained towards the right horizontally as quickly as the isotropic case, thus forcing the saturated region grows upwards.

Overall, together with previous examples, the last example of rainfall infiltration through an anisotropic slope presented above covers a wide range of transient unsaturated–saturated seepage flow problems that can be effectively solved by the newly proposed SPH framework. The excellent agreements achieved between SPH and other numerical methods (and/or existing numerical/analytical solutions) suggest that the new SPH model is generic and can be used to solve a wide range of transient seepage flow problems. Furthermore, the excellent agreements between SPH and other numerical methods, especially the last example involving anisotropic seepage flows, confirm that the newly proposed SPH formulation for the second derivatives is accurate and can be effectively used to solve anisotropic diffusion problems.

## 6. Conclusions

This paper presents a general SPH framework to solve anisotropic seepage problems in partially unsaturated porous media. To achieve this, a robust and general SPH formulation for the approximation of second derivatives is proposed and demonstrated to achieve high accuracy and outperform existing SPH formulations for the second derivatives, particularly on highly disordered particle systems, while sharing similar computational costs. Based on this newly developed SPH formulation, the general governing equations for the transient unsaturated/saturated seepage flows can be discretised and solved on a single set of SPH particles using simple boundary conditions. This new SPH framework stands out by its capability and computational efficiency in handling unsaturated/unsaturated seepage flow problems, comparing the existing SPH schemes adopting two layers of SPH particles [11,57]. It also addresses the existing challenges of FEM (as well as other mesh-based methods) in capturing seepage surface, which often requires ad-hoc or complex treatments to achieve reasonable results. Here, the new SPH model could automatically capture complex seepage surfaces without requiring any specific treatment. Furthermore, a simple method to generate a random particle system suitable for SPH simulations of large-scale problems using the Voronoi tessellation technique is also proposed to study transient seepage problems for the first time. Through several numerical verifications, it is demonstrated that the proposed SPH framework can accurately capture the evolution of pore-water pressure, water flow patterns and seepage surfaces for a wide range of problems using both uniform and non-uniform particle systems (or spatial discretisation). In particular, the complex seepage behaviour in a large earth dam embankment involving high inhomogeneity and complex geometry could also be well captured, thanks to the newly developed SPH formulation and the proposed Voronoi tessellation technique, which enables the proposed SPH framework to achieve excellent accuracy and efficiency on multi-resolution particle systems. Moreover, the newly developed SPH model was demonstrated to be able to accurately capture complex seepage flows through anisotropic porous media involving the full time-dependent transition from unsaturated state to fully saturated state.

Finally, it is important to note that the development of this new SPH framework for transient seepage flows will enable field-scale predictions of coupled flow-deformation involving large deformation and failure of porous media using SPH with minimal computational costs (i.e. using one set of particles and multi-resolution discretisation). An example of this type of application is rainfalls induced landslides or slope failures, which are challenging (if not impossible) for the most state-of-the-art mesh-based numerical methods while being relatively straightforward for SPH, thanks to its truly mesh-free nature. This coupling and results will be presented in our future work.

## Declaration of competing interest

The authors declare that they have no known competing financial interests or personal relationships that could have appeared to influence the work reported in this paper.

## Acknowledgements

The authors gratefully acknowledge support from the Australian Research Council via Discovery Projects DP170103793 (Nguyen, Bui), DP190102779 (Bui & Nguyen) and Future Fellow Project FT200100884 (Bui). Part of this research was undertaken with the assistance of resources and services from the National Computational Infrastructure (NCI), which is supported by the Australian Government. The support of the China Scholarship Council (CSC No. 201906050025) is also gratefully acknowledged.

## Appendix

This appendix shows the derivation of the stable CFL condition for solving the flow equation. Considering the non-linear PDE:

$$\frac{\partial v}{\partial t} = k \frac{\partial^2 v}{\partial x^2} \quad (\text{A.1})$$

where  $k$  is the diffusion coefficient;  $v$  could be any field variable. Rearranging the above equation into a differential form, which leads to:

$$v_i^{t+1} = v_i^t + \frac{k \Delta t}{\Delta x^2} (v_{i+1}^t - 2v_i^t + v_{i-1}^t) \quad (\text{A.2})$$

Now we imply the Von Neumann stability analysis. Assuming the numerical solution is  $v$ , and the analytical solution is  $U$ , then numerical error introduced by the computation process can be written as:

$$\epsilon_i^t = v_i^t - U_i^t \quad (\text{A.3})$$

Substitutive Eq. (A.3) into Eq. (A.2), leading to:

$$\begin{aligned} (U_i^{t+1} + \epsilon_i^{t+1}) &= (U_i^{t-1} + \epsilon_i^{t-1}) \\ &+ \frac{k\Delta t}{\Delta x^2} ((U_{i+1}^t + \epsilon_{i+1}^t) - 2(U_i^t + \epsilon_i^t) + (U_{i-1}^t + \epsilon_{i-1}^t)) \end{aligned} \quad (\text{A.4})$$

Given the  $U_i^t$  is the analytical solution, we can obtain:

$$(U_i^{t+1}) = (U_i^{t-1}) + \frac{k\Delta t}{\Delta x^2} ((U_{i+1}^t) - (U_{i-1}^t)) \quad (\text{A.5})$$

Subtracting Eq. (A.4) by Eq. (A.5), giving:

$$\epsilon_i^{t+1} = \epsilon_i^t + \frac{k\Delta t}{\Delta x^2} (\epsilon_{i+1}^t - 2\epsilon_i^t + \epsilon_{i-1}^t) \quad (\text{A.6})$$

If the error  $\epsilon_i$  exists in the system, when solving A1 from timestep  $t$  to  $t + 1$ , to ensure the iteration process's stabilisation,  $\epsilon_i$  must not increase. This condition can be expressed as

$$\xi^t = \left| \frac{\epsilon_i^{t+1}}{\epsilon_i^t} \right| \leq 1 \quad (\text{A.7})$$

Next, we will derive the condition that satisfies Eq. (A.7) from Eq. (A.6). The numerical error  $\epsilon_i$  can be expressed using **Fourier series** as follows:

$$\epsilon(x, t) = \sum_i \xi_i^t \exp(Iki\Delta x) \quad (\text{A.8})$$

where  $I = \sqrt{-1}$ . Just taking the first term of the Fourier series in the analysis, the computational error can be given as:

$$\epsilon_i^t = \xi^t \cdot \exp(Iki\Delta x) \quad (\text{A.9})$$

Substituting Eq. (A.9) into Eq. (A.6), leading to

$$\begin{aligned} \xi_i^{t+1} \exp(Iki\Delta x) &= \xi_i^t \exp(Iki\Delta x) \\ &+ \frac{k\Delta t}{\Delta x^2} (\xi_i^t \exp(Ik(i+1)\Delta x) - 2\xi_i^t \exp(Ik(i)\Delta x) \\ &+ \xi_i^t \exp(Ik(i-1)\Delta x)) \end{aligned} \quad (\text{A.10})$$

Dividing both sides by  $\xi^t \exp(Iki\Delta x)$  and using the identity  $\exp(a + bI) = \cos(b) + I \sin(b)$  which leads to:

$$\xi - 1 - \frac{k\Delta t}{\Delta x^2} (-2 + \cos(k\Delta x) + I \sin(I) + \cos(-k\Delta x) + I \sin(-k\Delta x)) = 0 \quad (\text{A.11})$$

Re-arranging the equation, which leads to:

$$\xi = 1 - \frac{k\Delta t}{\Delta x^2} \left( 4 \sin^2 \left( \frac{k\Delta x}{2} \right) \right) \quad (\text{A.12})$$

To satisfy the stable iteration condition, i.e.,  $|\xi| \leq 1$ , the following condition must be satisfied:

$$\begin{aligned} 1 - 4 \frac{k\Delta t}{\Delta x^2} \sin^2 \left( \frac{k\Delta x}{2} \right) &\geq -1 \\ 1 - 4 \frac{k\Delta t}{\Delta x^2} \sin^2 \left( \frac{k\Delta x}{2} \right) &\leq 1 \end{aligned} \rightarrow \begin{cases} \frac{k\Delta t}{\Delta x^2} \leq 0.5 \\ \frac{k\Delta t}{\Delta x^2} \geq 0 \end{cases} \quad (\text{A.13})$$

Therefore, when  $\frac{k\Delta t}{\Delta x^2} \in [0, \frac{1}{2}]$ ,  $|\xi| \leq 1$ , then the stable condition for Non-linear PDE can be expressed as:

$$\Delta t \leq \frac{\Delta x^2}{2k} \quad (\text{A.14})$$

Applying it to the seepage flow equations, the time step size for transient seepage can be evaluated as:

$$dt \leq \frac{\tilde{C}_{sr} dx^2}{2k_l} \quad (\text{A.15})$$

Replace the particle distance with the smoothing length, and noting the  $\frac{\tilde{C}_{sr} dx^2}{2k_l} \geq \frac{C_r h_{sml}^2}{k^{sat}}$ , we finally have the time-step for transient seepage flow:

$$dt \leq CFL \frac{\tilde{C}_{sr} h_{sml}^2}{k^{sat}} \quad (\text{A.16})$$

where  $CFL \in (0, 0.5)$  is the CFL factor.

Noting that for the unsaturated seepage flow, the time rate of the water pressure head is mainly governed by the moisture storage term, but by specific storage term in fully saturated condition. Therefore, generally for the transient seepage considering the transition from unsaturated to fully saturated, e.g. rainfall infiltration in unsaturated media, the system can have two time-step sizes determined by the unsaturated condition and fully saturated condition, respectively:

$$dt \leq \begin{cases} CFL \frac{\min(C_r^j) h_{sml}^2}{k^{sat}} & \text{Unsaturated} \quad (\text{a}) \\ CFL \frac{C_l h_{sml}^2}{k^{sat}} & \text{Saturated} \quad (\text{b}) \end{cases} \quad (\text{A.17})$$

Noting that the moisture storage term  $C_r^j$  varies with respect to the negative pore-water pressure head. Therefore, a minimum value was used to ensure the CFL condition is satisfied. In this case, before any particle in the computational domain goes into fully saturated condition (i.e. the pore water pressure greater than zero or the defined Air Entry Value), a large time-step size according to Eq. (A.17)(a) is used for the whole system. Once there is any particle satisfying the saturated condition, the time-step based on the Eq. (A.17)(b) will be adopted for the whole system. In this paper,  $CFL = 0.1$  is recommended.

## References

- [1] D.M. Pedroso, A solution to transient seepage in unsaturated porous media, Comput. Methods Appl. Mech. Engrg. 285 (2015) 791–816, <http://dx.doi.org/10.1016/j.cma.2014.12.009>.
- [2] H. Zheng, D.F. Liu, C.F. Lee, L.G. Tham, A new formulation of Signorini's type for seepage problems with free surfaces, Internat. J. Numer. Methods Engrg. 64 (2005) 1–16, <http://dx.doi.org/10.1002/nme.1345>.
- [3] H. Zheng, H.C. Dai, D.F. Liu, A variational inequality formulation for unconfined seepage problems in porous media, Appl. Math. Model. 33 (2009) 437–450, <http://dx.doi.org/10.1016/j.apm.2007.11.012>.
- [4] S.J. Lacy, J.H. Prevost, Flow through porous media: A procedure for locating the free surface, Int. J. Numer. Anal. Methods Geomech. 11 (1987) 585–601, <http://dx.doi.org/10.1002/nag.1610110605>.
- [5] R.I. Borja, S.S. Kishnani, On the solution of elliptic free-boundary problems via Newton's method, Comput. Methods Appl. Mech. Engrg. 88 (1991) 341–361, [http://dx.doi.org/10.1016/0045-7825\(91\)90094-M](http://dx.doi.org/10.1016/0045-7825(91)90094-M).
- [6] J.T. Oden, N. Kikuchi, Theory of variational inequalities with applications to problems of flow through porous media, Internat. J. Engrg. Sci. 18 (1980) 1173–1284, [http://dx.doi.org/10.1016/0020-7225\(80\)90111-1](http://dx.doi.org/10.1016/0020-7225(80)90111-1).
- [7] K.K. Lee, D.I. Leap, Simulation of a free-surface and seepage face using boundary-fitted coordinate system method, J. Hydrol. 196 (1997) 297–309, [http://dx.doi.org/10.1016/S0022-1694\(96\)03246-5](http://dx.doi.org/10.1016/S0022-1694(96)03246-5).
- [8] J.P. Bardet, T. Tobita, A practical method for solving free-surface seepage problems, Comput. Geotech. 29 (2002) 451–475, [http://dx.doi.org/10.1016/S0266-352X\(02\)00003-4](http://dx.doi.org/10.1016/S0266-352X(02)00003-4).
- [9] H. Brezis, Sur une nouvelle formulation du probleme de l'ecoulement a travers une digue, C. R. Acad. Sci. Paris 287 (1978) 711–714, <https://ci.nii.ac.jp/naid/80013858036> (accessed May 17, 2021).
- [10] M.I. Herreros, M. Mabsout, M. Pastor, Application of level-set approach to moving interfaces and free surface problems in flow through porous media, Comput. Methods Appl. Mech. Engrg. 195 (2006) 1–25, <http://dx.doi.org/10.1016/j.cma.2004.12.015>.
- [11] H.H. Bui, G.D. Nguyen, A coupled fluid-solid SPH approach to modelling flow through deformable porous media, Int. J. Solids Struct. 125 (2017) 244–264, <http://dx.doi.org/10.1016/j.ijsolstr.2017.06.022>.
- [12] L.B. Lucy, A numerical approach to the testing of the fission hypothesis, 82 (1977) 1013–1024.

- [13] A.R. Gingold, J.J. Monaghan, Smoothed particle hydrodynamics: theory and application to non-spherical stars, 181 (1977) 375–389.
- [14] S. Härdi, M. Schreiner, U. Janoske, Enhancing smoothed particle hydrodynamics for shallow water equations on small scales by using the finite particle method, Comput. Methods Appl. Mech. Engrg. 344 (2019) 360–375, <http://dx.doi.org/10.1016/j.cma.2018.10.021>.
- [15] K. Liu, Y. Wang, M. Huang, W.-H. Yuan, Postfailure analysis of slopes by random generalized interpolation material point method, Int. J. Geomech. 21 (2021) 04021015, [http://dx.doi.org/10.1061/\(asce\)gm.1943-5622.0001953](http://dx.doi.org/10.1061/(asce)gm.1943-5622.0001953).
- [16] W. Hu, W. Pan, M. Rakhsha, Q. Tian, H. Hu, D. Negrut, A consistent multi-resolution smoothed particle hydrodynamics method, Comput. Methods Appl. Mech. Engrg. 324 (2017) 278–299, <http://dx.doi.org/10.1016/j.cma.2017.06.010>.
- [17] A. Tafuni, J.M. Domínguez, R. Vacondio, A.J.C. Crespo, A versatile algorithm for the treatment of open boundary conditions in smoothed particle hydrodynamics GPU models, Comput. Methods Appl. Mech. Engrg. 342 (2018) 604–624, <http://dx.doi.org/10.1016/j.cma.2018.08.004>.
- [18] A. Khayyer, H. Gotoh, Y. Shimizu, Comparative study on accuracy and conservation properties of two particle regularization schemes and proposal of an optimized particle shifting scheme in ISPH context, J. Comput. Phys. 332 (2017) 236–256, <http://dx.doi.org/10.1016/j.jcp.2016.12.005>.
- [19] D. Morikawa, H. Senadheera, M. Asai, Explicit incompressible smoothed particle hydrodynamics in a multi-GPU environment for large-scale simulations, Comput. Part. Mech. 8 (2021) 493–510, <http://dx.doi.org/10.1007/s40571-020-00347-0>.
- [20] Z. Ji, L. Fu, X.Y. Hu, N.A. Adams, A new multi-resolution parallel framework for SPH, Comput. Methods Appl. Mech. Engrg. 346 (2019) 1156–1178, <http://dx.doi.org/10.1016/j.cma.2018.09.043>.
- [21] X.Y. Hu, N.A. Adams, An incompressible multi-phase SPH method, J. Comput. Phys. 227 (2007) 264–278, <http://dx.doi.org/10.1016/j.jcp.2007.07.013>.
- [22] D.S. Morikawa, M. Asai, Coupling total Lagrangian SPH–EISPH for fluid–structure interaction with large deformed hyperelastic solid bodies, Comput. Methods Appl. Mech. Engrg. 381 (2021) 113832, <http://dx.doi.org/10.1016/j.cma.2021.113832>.
- [23] A. Monteleone, M. De Marchis, B. Milici, E. Napoli, A multi-domain approach for smoothed particle hydrodynamics simulations of highly complex flows, Comput. Methods Appl. Mech. Engrg. 340 (2018) 956–977, <http://dx.doi.org/10.1016/j.cma.2018.06.029>.
- [24] M. Rakhsha, A. Pazouki, R. Serban, D. Negrut, Using a half-implicit integration scheme for the SPH-based solution of fluid–solid interaction problems, Comput. Methods Appl. Mech. Engrg. 345 (2019) 100–122, <http://dx.doi.org/10.1016/j.cma.2018.09.027>.
- [25] C. Antoci, M. Gallati, S. Sibilla, Numerical simulation of fluid–structure interaction by SPH, Comput. Struct. 85 (2007) 879–890, <http://dx.doi.org/10.1016/j.compstruc.2007.01.002>.
- [26] A. Khayyer, Y. Shimizu, H. Gotoh, K. Nagashima, A coupled incompressible SPH-Hamiltonian SPH solver for hydroelastic FSI corresponding to composite structures, Appl. Math. Model. 94 (2021) 242–271, <http://dx.doi.org/10.1016/j.apm.2021.01.011>.
- [27] A. Khayyer, Y. Shimizu, H. Gotoh, S. Hattori, Multi-resolution ISPH-SPH for accurate and efficient simulation of hydroelastic fluid–structure interactions in ocean engineering, Ocean Eng. 226 (2021) 108652, <http://dx.doi.org/10.1016/j.oceaneng.2021.108652>.
- [28] Z.L. Zhang, T. Long, J.Z. Chang, M.B. Liu, A smoothed particle element method (SPEM) for modeling fluid–structure interaction problems with large fluid deformations, Comput. Methods Appl. Mech. Engrg. 356 (2019) 261–293, <http://dx.doi.org/10.1016/j.cma.2019.07.024>.
- [29] M. Asai, Y. Li, B. Chandra, S. Takase, Fluid–rigid-body interaction simulations and validations using a coupled stabilized ISPH–DEM incorporated with the energy-tracking impulse method for multiple-body contacts, Comput. Methods Appl. Mech. Engrg. 377 (2021) 113681, <http://dx.doi.org/10.1016/j.cma.2021.113681>.
- [30] C. Zhang, M. Rezavand, X. Hu, A multi-resolution SPH method for fluid–structure interactions, J. Comput. Phys. 429 (2021) <http://dx.doi.org/10.1016/j.jcp.2020.110028>.
- [31] K. Ba, A. Gakwaya, Thermomechanical total Lagrangian SPH formulation for solid mechanics in large deformation problems, Comput. Methods Appl. Mech. Engrg. 342 (2018) 458–473, <http://dx.doi.org/10.1016/j.cma.2018.07.038>.
- [32] H.H. Bui, R. Fukagawa, K. Sako, S. Ohno, Lagrangian meshfree particles method (SPH) for large deformation and failure flows of geomaterial using elastic–plastic soil constitutive model, Int. J. Numer. Anal. Methods Geomech. 32 (2008) 1537–1570, <http://dx.doi.org/10.1002/nag>.
- [33] C.T. Nguyen, C.T. Nguyen, H.H. Bui, G.D. Nguyen, R. Fukagawa, A new SPH-based approach to simulation of granular flows using viscous damping and stress regularisation, Landslides 14 (2017) 69–81, <http://dx.doi.org/10.1007/s10346-016-0681-y>.
- [34] C.M. Chalk, M. Pastor, J. Peakall, D.J. Borman, P.A. Sleigh, W. Murphy, R. Fuentes, Stress-particle smoothed particle hydrodynamics: An application to the failure and post-failure behaviour of slopes, Comput. Methods Appl. Mech. Engrg. 366 (2020) <http://dx.doi.org/10.1016/j.cma.2020.113034>.
- [35] R.I. Borja, Continuum hydrodynamics of dry granular flows employing multiplicative elastoplasticity, 3 (2018). <http://dx.doi.org/10.1007/s11440-018-0700-3>.
- [36] E. Yang, H.H. Bui, H. De Sterck, G.D. Nguyen, A. Bouazza, A scalable parallel computing SPH framework for predictions of geophysical granular flows, Comput. Geotech. 121 (2020) 103474, <http://dx.doi.org/10.1016/j.comgeo.2020.103474>.
- [37] A.H. Fávero Neto, A. Askarinejad, S.M. Springman, R.I. Borja, Simulation of debris flow on an instrumented test slope using an updated Lagrangian continuum particle method, Acta Geotech. 15 (2020) 2757–2777, <http://dx.doi.org/10.1007/s11440-020-00957-1>.
- [38] C. Huang, M.B. Liu, Modeling hydrate-bearing sediment with a mixed smoothed particle hydrodynamics, Comput. Mech. 66 (2020) 877–891, <http://dx.doi.org/10.1007/s00466-020-01895-1>.
- [39] H.H. Bui, R. Fukagawa, K. Sako, J.C. Wells, Slope stability analysis and discontinuous slope failure simulation by elasto-plastic smoothed particle hydrodynamics (SPH), Geotechnique 61 (2011) 565–574, <http://dx.doi.org/10.1680/geot.9.P.046>.
- [40] X. He, D. Liang, M.D. Bolton, Run-out of cut-slope landslides: Mesh-free simulations, Geotechnique 68 (2018) 50–63, <http://dx.doi.org/10.1680/geot.16.P.221>.

- [41] H.H. Bui, R. Fukagawa, An improved SPH method for saturated soils and its application to investigate the mechanisms of embankment failure: Case of hydrostatic pore-water pressure, *Int. J. Numer. Anal. Methods Geomech.* 37 (2013) 31–50, <http://dx.doi.org/10.1002/nag.1084>.
- [42] M. Pastor, T. Blanc, B. Haddad, S. Petrone, M. Sanchez Morles, V. Drempetic, D. Issler, G.B. Crosta, L. Cascini, G. Sorbino, S. Cuomo, Application of a SPH depth-integrated model to landslide run-out analysis, *Landslides* 11 (2014) 793–812, <http://dx.doi.org/10.1007/s10346-014-0484-y>.
- [43] T. Blanc, M. Pastor, A stabilized runge-kutta, taylor smoothed particle hydrodynamics algorithm for large deformation problems indynamics, *Internat. J. Numer. Methods Engrg.* 91 (2012) 1427–1458, <http://dx.doi.org/10.1002/nme.4324>.
- [44] S. Zhao, H.H. Bui, V. Lemiale, G.D. Nguyen, F. Darve, A generic approach to modelling flexible confined boundary conditions in SPH and its application, *Int. J. Numer. Anal. Methods Geomech.* 43 (2019) 1005–1031, <http://dx.doi.org/10.1002/nag.2918>.
- [45] W. Chen, T. Qiu, Simulation of earthquake-induced slope deformation using SPH method, *Int. J. Numer. Anal. Methods Geomech.* 38 (2014) 297–330, <http://dx.doi.org/10.1002/nag.2218>.
- [46] E. Yang, H.H. Bui, G.D. Nguyen, C.E. Choi, C.W.W. Ng, H. De Sterck, A. Bouazza, Numerical investigation of the mechanism of granular flow impact on rigid control structures, *Acta Geotech.* (2021) <http://dx.doi.org/10.1007/s11440-021-01162-4>.
- [47] L. Zhan, C. Peng, B. Zhang, W. Wu, A SPH framework for dynamic interaction between soil and rigid body system with hybrid contact method, *Int. J. Numer. Anal. Methods Geomech.* 44 (2020) 1446–1471, <http://dx.doi.org/10.1002/nag.3070>.
- [48] B. Sheikh, T. Qiu, A. Ahmadipur, Comparison of SPH boundary approaches in simulating frictional soil–structure interaction, *Acta Geotech.* (2020) 1–20, <http://dx.doi.org/10.1007/s11440-020-01063-y>.
- [49] H.H. Bui, J.K. Kodikara, A. Bouazza, A. Haque, P.G. Ranjith, A novel computational approach for large deformation and post-failure analyses of segmental retaining wall systems, *Int. J. Numer. Anal. Methods Geomech.* 38 (2014) 1321–1340, <http://dx.doi.org/10.1002/nag.2253>.
- [50] H.T. Tran, Y. Wang, G.D. Nguyen, J. Kodikara, M. Sanchez, H.H. Bui, Modelling 3D desiccation cracking in clayey soils using a size-dependent SPH computational approach, *Comput. Geotech.* 116 (2019) 103209, <http://dx.doi.org/10.1016/j.compgeo.2019.103209>.
- [51] H.T. Tran, N.H.T. Nguyen, G.D. Nguyen, H.H. Bui, Meshfree SPH modelling of shrinkage induced cracking in clayey soils, *Lect. Notes Civ. Eng.* 54 (2020) 889–894, [http://dx.doi.org/10.1007/978-981-15-0802-8\\_142](http://dx.doi.org/10.1007/978-981-15-0802-8_142).
- [52] Y. Wang, H.T. Tran, G.D. Nguyen, P.G. Ranjith, H.H. Bui, Simulation of mixed-mode fracture using SPH particles with an embedded fracture process zone, *Int. J. Numer. Anal. Methods Geomech.* 44 (2020) 1417–1445, <http://dx.doi.org/10.1002/nag.3069>.
- [53] Y. Wang, H.H. Bui, G.D. Nguyen, P.G. Ranjith, A new SPH-based continuum framework with an embedded fracture process zone for modelling rock fracture, *Int. J. Solids Struct.* 159 (2019) 40–57, <http://dx.doi.org/10.1016/j.ijsolstr.2018.09.019>.
- [54] S. Gharehdash, L. Shen, Y. Gan, Numerical study on mechanical and hydraulic behaviour of blast-induced fractured rock, *Eng. Comput.* 36 (2020) 915–929, <http://dx.doi.org/10.1007/s00366-019-00740-1>.
- [55] T. Blanc, M. Pastor, A stabilized Fractional Step, Runge–Kutta Taylor SPH algorithm for coupled problems in geomechanics, *Comput. Methods Appl. Mech. Engrg.* 221–222 (2012) 41–53, <http://dx.doi.org/10.1016/j.cma.2012.02.006>.
- [56] E. Kermani, T. Qiu, Simulation of Seepage through Fixed Porous Media Using the Smoothed Particle Hydrodynamics Method, American Society of Civil Engineers (ASCE), 2017, pp. 699–708, <http://dx.doi.org/10.1061/9780784480472.074>.
- [57] H.H. Bui, K. Sako, R. Fukagawa, Numerical simulation of soil–water interaction using smoothed particle hydrodynamics (SPH) method, *J. Terramech.* 44 (2007) 339–346, <http://dx.doi.org/10.1016/j.jterra.2007.10.003>.
- [58] L. Brookshaw, A method of calculating radiative heat diffusion in particle simulations, *Astron. Soc. Aust.* 6 (1985) 207–210.
- [59] P.W. Cleary, J.J. Monaghan, Conduction modelling using smoothed particle hydrodynamics, *J. Comput. Phys.* 148 (1999) 227–264, <http://dx.doi.org/10.1006/jcph.1998.6118>.
- [60] J.J. Monaghan, Smoothed particle hydrodynamics, *Rep. Progr. Phys.* 68 (2005) 1703–1759, <http://dx.doi.org/10.1088/0034-4885/68/8/R01>.
- [61] P. Español, M. Revenga, Smoothed dissipative particle dynamics, *Phys. Rev. E* 67 (2003) 12, <http://dx.doi.org/10.1103/PhysRevE.67.026705>.
- [62] M. Petkova, V. Springel, An implementation of radiative transfer in the cosmological simulation code gadget, *Mon. Not. R. Astron. Soc.* 396 (2009) 1383–1403, <http://dx.doi.org/10.1111/j.1365-2966.2009.14843.x>.
- [63] P.F. Hopkins, Anisotropic diffusion in mesh-free numerical magnetohydrodynamics, *Mon. Not. R. Astron. Soc.* 466 (2017) 3387–3405, <http://dx.doi.org/10.1093/mnras/stw3306>.
- [64] J.K. Chen, J.E. Beraun, T.C. Carney, A corrective smoothed particle method for boundary value problems in heat conduction, *Internat. J. Numer. Methods Engrg.* 46 (1999) 231–252, [http://dx.doi.org/10.1002/\(SICI\)1097-0207\(19990920\)46:2<231::AID-NME672>3.0.CO;2-K](http://dx.doi.org/10.1002/(SICI)1097-0207(19990920)46:2<231::AID-NME672>3.0.CO;2-K).
- [65] H.H. Bui, G.D. Nguyen, Smoothed particle hydrodynamics (SPH) and its applications in geomechanics: from solid fracture to granular behaviour and multiphase flows in porous media, *Comput. Geotech.* 138 (2021) 104315, <http://dx.doi.org/10.1016/j.compgeo.2021.104315>.
- [66] R. Fatehi, M.T. Manzari, Error estimation in smoothed particle hydrodynamics and a new scheme for second derivatives, *Comput. Math. Appl.* 61 (2011) 482–498, <http://dx.doi.org/10.1016/j.camwa.2010.11.028>.
- [67] S. Diehl, G. Rockefeller, C.L. Fryer, D. Riethmiller, T.S. Statler, Generating optimal initial conditions for smoothed particle hydrodynamics simulations, *Publ. Astron. Soc. Aust.* 32 (2015) <http://dx.doi.org/10.1017/pasa.2015.50>.
- [68] S. Heß, V. Springel, Particle hydrodynamics with tessellation techniques, *Mon. Not. R. Astron. Soc.* 406 (2010) 2289–2311, <http://dx.doi.org/10.1111/j.1365-2966.2010.16892.x>.
- [69] M.A. Ghaffari, S. Xiao, Smoothed particle hydrodynamics with stress points and centroid voronoi tessellation (CVT) topology optimization, *Int. J. Comput. Methods* 13 (2016) 1–23, <http://dx.doi.org/10.1142/S0219876216500316>.

- [70] G. Shobeyri, R.R. Ardakani, Improving accuracy of SPH method using voronoi diagram, *Iran. J. Sci. Technol. - Trans. Civ. Eng.* 41 (2017) 345–350, <http://dx.doi.org/10.1007/s40996-017-0069-9>.
- [71] X. Bian, Z. Li, G.E. Karniadakis, Multi-resolution flow simulations by smoothed particle hydrodynamics via domain decomposition, *J. Comput. Phys.* 297 (2015) 132–155, <http://dx.doi.org/10.1016/j.jcp.2015.04.044>.
- [72] F. Oka, B. Shahbodagh, S. Kimoto, A computational model for dynamic strain localization in unsaturated elasto-viscoplastic soils, *Int. J. Numer. Anal. Methods Geomech.* 43 (2019) 138–165, <http://dx.doi.org/10.1002/nag.2857>.
- [73] F. Oka, T. Kodaka, H. Suzuki, Y.S. Kim, N. Nishimatsu, S. Kimoto, Experimental study on the behavior of unsaturated compacted silt under triaxial compression, *Soils Found.* 50 (2010) 27–44, <http://dx.doi.org/10.3208/sandf.50.27>.
- [74] J. Bear, A.H.-D. Cheng, Modeling Groundwater Flow and Contaminant Transport, 2010, <http://dx.doi.org/10.1007/978-1-4020-6682-5>.
- [75] M.T. van Genuchten, A closed-form equation for predicting the hydraulic conductivity of unsaturated soils, *Soil Sci. Soc. Am. J.* 44 (1980) 892–898, <http://dx.doi.org/10.2136/sssaj1980.03615995004400050002x>.
- [76] J.J. Monaghan, Extrapolating B splines for interpolation, *J. Comput. Phys.* 60 (1985) 253–262, [http://dx.doi.org/10.1016/0021-9991\(85\)90006-3](http://dx.doi.org/10.1016/0021-9991(85)90006-3).
- [77] G. Oger, M. Doring, B. Alessandrini, P. Ferrant, An improved SPH method: Towards higher order convergence, *J. Comput. Phys.* 225 (2007) 1472–1492, <http://dx.doi.org/10.1016/j.jcp.2007.01.039>.
- [78] P.W. Randles, L.D. Libersky, Smoothed particle hydrodynamics: Some recent improvements and applications, *Comput. Methods Appl. Mech. Engrg.* 139 (1996) 375–408, [http://dx.doi.org/10.1016/S0045-7825\(96\)01090-0](http://dx.doi.org/10.1016/S0045-7825(96)01090-0).
- [79] J.K. Chen, J.E. Beraun, A generalized smoothed particle hydrodynamics method for nonlinear dynamic problems, *Comput. Methods Appl. Mech. Engrg.* 190 (2000) 225–239, [http://dx.doi.org/10.1016/S0045-7825\(99\)00422-3](http://dx.doi.org/10.1016/S0045-7825(99)00422-3).
- [80] Q. Du, V. Faber, M. Gunzburger, Centroidal Voronoi tessellations: Applications and algorithms, *SIAM Rev.* 41 (1999) 637–676, <http://dx.doi.org/10.1137/S0036144599352836>.
- [81] C. Talischi, G.H. Paulino, A. Pereira, I.F.M. Menezes, PolyMesher: A general-purpose mesh generator for polygonal elements written in matlab, *Struct. Multidiscip. Optim.* 45 (2012) 309–328, <http://dx.doi.org/10.1007/s00158-011-0706-z>.
- [82] S.P. Lloyd, Least squares quantization in PCM, *IEEE Trans. Inf. Theory* 28 (1982) 129–137, <http://dx.doi.org/10.1109/TIT.1982.1056489>.
- [83] M.B. Liu, G.R. Liu, Smoothed particle hydrodynamics (SPH): An overview and recent developments, *Arch. Comput. Methods Eng.* 17 (2010) 25–76, <http://dx.doi.org/10.1007/s11831-010-9040-7>.
- [84] H.H. Bui, Lagrangian Mesh-Free Particle Method (SPH) for Large Deformation and Post-Failure of Geomaterial using Elasto-Plastic Constitutive Models (Doctoral dissertation), Ritsumeikan Univ., 2006, [http://r-cube.ritsumei.ac.jp/repo/repository/rcube/9152/k\\_466\\_e.htm](http://r-cube.ritsumei.ac.jp/repo/repository/rcube/9152/k_466_e.htm).
- [85] W.R. Gardner, Some steady-state solutions of the unsaturated moisture flow equation with application to evaporation from a water table, *Soil Sci.* 85 (1958) 228–232, <http://dx.doi.org/10.1097/00010694-195804000-00006>.
- [86] P.J. Polubarnova-Kochina, R.J.M. De Wiest, Theory of Ground Water Movement, Princeton Univ. Press, 1962, <https://lib.ugent.be/catalog/rug01:000200814> (accessed May 16, 2021).